

# Powering Electronic Implants by High Frequency Volume Conduction: In Human Validation

Jesus Minguillon, Marc Tudela-Pi, Laura Becerra-Fajardo, *Member, IEEE*, Enric Perera-Bel, Antonio J. del-Ama, Ángel Gil-Agudo, Álvaro Megía-García, Aracelys García-Moreno, Antoni Ivorra\*, *Member, IEEE*

**Abstract—Objective:** Wireless power transfer (WPT) is used as an alternative to batteries to accomplish miniaturization in electronic medical implants. However, established WPT methods require bulky parts within the implant or cumbersome external systems, hindering minimally invasive deployments and the development of networks of implants. As an alternative, we propose a WPT approach based on volume conduction of high frequency (HF) current bursts. These currents are applied through external electrodes and are collected by the implants through two electrodes at their opposite ends. This approach avoids bulky components, enabling the development of flexible threadlike implants. **Methods:** We study in humans if HF (6.78 MHz) current bursts complying with safety standards and applied through two textile electrodes strapped around a limb can provide substantial powers from pairs of implanted electrodes. **Results:** Time averaged electric powers obtained from needle electrodes (diameter = 0.4 mm, length = 3 mm, separation = 30 mm) inserted into arms and lower legs of five healthy participants were  $5.9 \pm 0.7$  mW and  $2.4 \pm 0.3$  mW respectively. We also characterize the coupling between the external system and the implants using personalized two-port impedance models generated from medical images. **Conclusions:** The results demonstrate that innocuous and imperceptible HF current bursts that flow through the tissues by volume conduction can be used to wirelessly power threadlike implants. **Significance:** This is the first time that WPT based on volume conduction is demonstrated in humans. This method overcomes the limitations of existing WPT methods in terms of minimal invasiveness and usability.

**Index Terms**—galvanic coupling, human validation, implantable biomedical devices, volume conduction, wireless power transfer.

## I. INTRODUCTION

WIRELESS power transfer (WPT) is frequently used in electronic medical implants as an alternative to electrochemical batteries. WPT offers two major advantages for the implant: longevity and miniaturization. In addition to electrochemical batteries and nuclear batteries [1], other intrinsic power mechanisms have been explored such as those labeled as energy scavengers or energy harvesters [2]–[6]. However, all these alternative intrinsic power generation mechanisms also require voluminous parts (e.g., oscillating weights or thermopiles) to be integrated within the implants and provide powers considered to be insufficient for most implanted devices [7].

To the best of our knowledge, the only WPT methods in clinical use are near-field inductive coupling and ultrasonic acoustic coupling [8], the former being much more prevalent than the latter. Other WPT methods under exploration are: optic WPT [9]–[13], mid-field inductive coupling [14], [15], far-field coupling [16], capacitive coupling [17]–[19] and WPT based on volume conduction which is also, less accurately, referred to as galvanic coupling [20]–[24]. Comprehensive and partial recent reviews on these methods can be found in [25]–[28].

Compared to other WPT methods, galvanic coupling and capacitive coupling offer the advantage of not requiring a cumbersome external system or integrating bulky parts, such as piezoelectric crystals or coils, within the receiving implant for absorbing the energy transferred by the remote transmitter. The energy can be readily picked-up with a pair of thin electrodes separated by a few millimeters or centimeters. In addition, galvanic coupling and capacitive coupling are compatible with metallic hermetic packages (for housing the electronics) that can be made thinner than their glass or ceramic counterparts.

By using WPT based on high frequency (HF) volume conduction, we envision the development of injectable devices such as the one illustrated in Fig. 1a. That is, we envision

Manuscript received March 22, 2022; revised July 26, 2022; accepted August 14, 2022. This work was supported by the European Union's Horizon 2020 Research and Innovation Programme under Grant 779982. A. Ivorra gratefully acknowledges the financial support by ICREA under the ICREA Academia Programme.

J. Minguillon, M. Tudela-Pi, L. Becerra-Fajardo, E. Perera-Bel, and A. García-Moreno are with the Dept. of Information and Communications Technologies, Universitat Pompeu Fabra, Barcelona, Spain. A. J. del Ama is with the Electronic Technology Area, Rey Juan Carlos University, Mostoles, Spain. Á. Gil-Agudo and Á. Megía-García are with the Dept. of Biomechanics and Technical Aids, National Hospital for Paraplegics, Toledo, Spain. \*A. Ivorra is with the Serra Hünter Fellow Programme, Dept. of Information and Communications Technologies, Universitat Pompeu Fabra, Barcelona, Spain (correspondence e-mail: antoni.ivorra@upf.edu).

Copyright (c) 2021 IEEE. Personal use of this material is permitted. However, permission to use this material for any other purposes must be obtained from the IEEE by sending an email to pubs-permissions@ieee.org.

implantable devices with a diameter below 1 mm which consist of a very thin flexible body with two electrodes at opposite ends and a hermetic capsule with electronics within the flexible body. Because of their thinness and flexibility, it will be possible to implant these devices through minimally invasive procedures such as injection (as we have already demonstrated in [29]) or catheterization.

In the context of WPT for electronic medical implants, the distinction between galvanic coupling and capacitive coupling is fuzzy. In both cases the transmitter generates an alternating electric field across two electrodes and this field is picked-up by two electrodes of the receiver. The term galvanic coupling is generally employed when the transmitter electrodes and the receiver electrodes are directly in contact with the tissues (without any sort of insulation) and the frequencies are not very high ( $< 100$  MHz). On the other hand, the term capacitive coupling is generally employed when the electrodes are coated with a dielectric and the frequencies are very high ( $> 100$  MHz). Due to the passive electrical properties of living tissues, neither outright conductors nor outright dielectrics, in both cases the ac currents that flow through the tissues have a real component (corresponding to conduction currents, hence the term galvanic coupling) and an imaginary component (corresponding to displacement currents). The term volume conduction, therefore, is more accurate than the terms galvanic or capacitive coupling since both mechanisms are typically acting at the same time. We advocate for the use of frequencies in the order of some MHz or a very few tens of MHz to be able to power deep implants by avoiding the skin effect which in living tissues is very significant at frequencies above 100 MHz [30]. At the frequencies we propose, the conduction currents are substantially higher than the displacement currents and hence the use of the term galvanic coupling is justified [22].

Remarkably, although galvanic coupling for intrabody communications has been studied lately by different research groups [31]–[33] and it is even employed in implants in clinical use [34], it appears that recently only in a very few occasions, besides in our own publications [20], [22], its use for powering implants has been explicitly proposed [21], [23], [35], [36]. To this group can be added a few studies in which volume conduction at frequencies substantially below 100 MHz was proposed albeit referred to as capacitive coupling [18], [37]–[39]. The absence of clinical systems using volume conduction for WPT is noteworthy, particularly taking into account that volume conduction for powering implanted devices was proposed more than 50 years ago [40]. We conjecture that such neglect mainly arises from not recognizing two crucial opportunities granted by volume conduction. First, large magnitude HF currents can safely flow through the human body if applied as short bursts (i.e., short enough to keep the overall power under the safety limit) [41]. Second, to obtain a sufficient voltage drop across its two intake (pick-up) electrodes, the implant can be shaped as a thin and flexible threadlike body (Fig. 1b) which, as already stated, is a conformation suitable for minimally invasive deployment

through injection or catheterization. Indeed, a singular feature of the conformation we propose to perform WPT based on volume conduction is the avoidance of flat structures for the receiver electrodes in the implant. Other researchers have typically proposed flat electrodes with a large surface area for maximizing power transfer efficiency, particularly in setups where the receiver electrodes are very close to the transmitter electrodes [35], [42]. However, the use of large flat electrodes, albeit thin, precludes implantation via minimally invasive procedures and, therefore, results in systems which in terms of clinical applicability are similar to those based on inductive coupling. It can be stated that we trade power transfer efficiency off for minimal invasiveness.

It is worth noting that conduction through the human body is also proposed to power wearable devices [43]–[46]. In these cases, however, the transmitter is not intended to generate an electric field within tissues; the body is used to close a circuit in which the devices are actually coupled through parasitic capacitances (in most cases through earth). The term body-coupling is frequently used to refer to this approach. Typically, even using relatively large devices for achieving substantial coupling capacitances, the powers attainable by this approach are in the orders of tens of  $\mu\text{W}$  [45].

The main goal of the present study is to illustrate that large magnitude HF currents can be innocuously and imperceptibly applied to humans and to demonstrate that those currents can produce substantial electric powers when picked-up by a pair of thin intramuscular electrodes separated a very few centimeters. The innocuity of the applied currents is ensured by adhering to available international safety standards for human exposure to electromagnetic fields [47], [48]. In the present study, the IEEE standard [48] was followed. The frequency of the applied sinusoidal currents (modulated as bursts) was set to 6.78 MHz because it corresponds to the central frequency of a designated ISM band [49], thus minimizing the possibility of interfering radiocommunication systems, and because it is high enough to easily avoid risks related to unsought electrostimulation.

In the present study, we report the results of the first in human validation of WPT based on HF volume conduction for implants. Previous studies done by others and by us using different implant geometries were performed *in silico*, *in vivo* or *ex vivo*, but never in humans. In addition, we propose and validate a procedure to model this WPT method, which characterizes coupling between the transmitters (i.e., external system) and the receivers (i.e., implants) by means of personalized two-port impedance models generated from participants' medical images. We previously studied and validated the two-port network model *in vitro* [50] and *in silico* [51]. However, in this work we validate the model in humans using different real anatomies. This procedure is not only relevant for the design of systems using WPT based on volume conduction, but it could also be applied for modeling transmission channels in intrabody communications based on volume conduction.

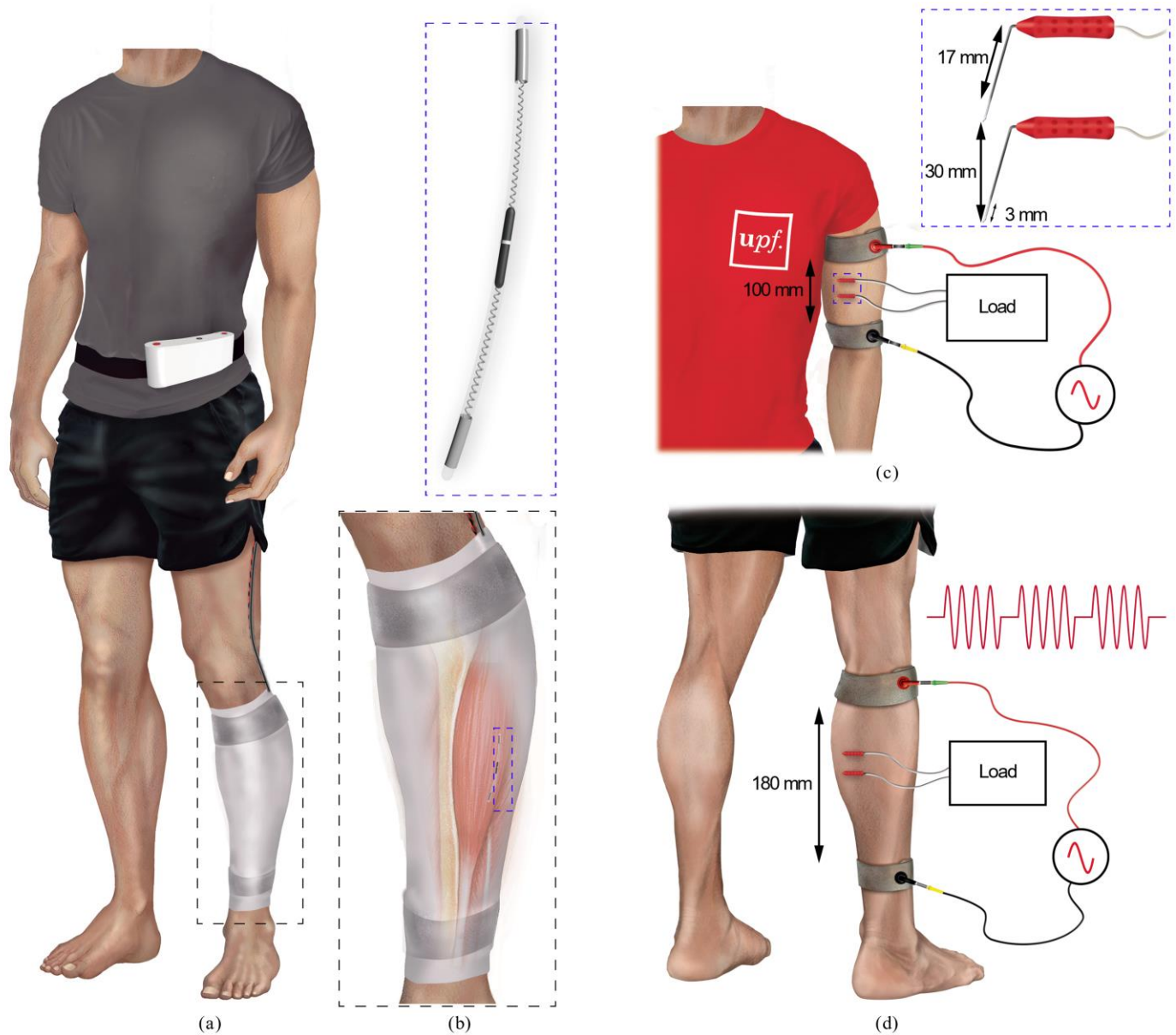


Fig. 1. Hypothetical scenario of use for wireless power transfer (WPT) based on high frequency volume conduction and experimental setups employed in the present study. (a) Hypothetical scenario: an elongated threadlike implant (e.g., for neuromuscular electrical stimulation of the tibialis anterior in foot drop patients[52]) is powered by high frequency current bursts that are applied by a portable generator through a pair of external textile electrodes. (b) Enlarged view of the implant, and its location in the tibialis anterior muscle. (c) Upper limb (arm) experimental setup: an external electrical load (resistive) is connected to a pair of needle electrodes inserted into the brachial biceps. (d) Lower limb (lower leg) experimental setup.

## II. METHODS

### A. Participants

Five young (age range from 21 to 38 years) healthy volunteers participated in the study: P1 (female), P2 (female), P3 (female), P4 (male) and P5 (male). They were recruited through a call for participation sent by email to colleagues and were not paid for their participation. Before starting the experimental procedure, they were provided with oral and written information regarding the study (including risks, benefits, and data protection aspects) and signed an informed consent form. The study was conducted in the National Hospital for Paraplegics in Toledo (Spain). The experimental protocol was approved by the Ethics Committee for Clinical

Investigation of the Complejo Hospitalario de Toledo (December 5, 2019; reference number: 467).

### B. Experimental Procedures

The experimental procedures were divided into two phases. During the first phase, magnetic resonance imaging (MRI) sequences were acquired for the non-dominant arm and lower leg of each participant. These images were used to build 3D computational models for numerical calculations (see Section II.C). Prior to MRI acquisition, the planned locations for the external and for the intramuscular electrodes were marked by drawing crosses using a permanent ink marker. Then, MRI fiducial markers (PinPoint® for Small Field of View Imaging 187 from Beekley Corporation, Bristol, CT, US) were placed over the marks. Two MRI markers were used for the needle

electrodes per participant and limb (i.e., one per needle) and three for each band. The position of the participants during MRI acquisition was the same as that during the second phase of the experimental procedures. Once all the participants finished the first phase, they sequentially participated in the second phase. During the second phase, different procedures and assays were conducted. First, the participant was positioned on a stretcher (supine and prone positions for arm and lower leg, respectively) and instructed to avoid unnecessary movements. A pair of external electrodes was strapped around the corresponding limb. As control, another pair of electrodes was strapped around the contralateral limb for later discerning whether skin alterations could be due to the delivery of the HF currents or were caused by the materials of the electrodes. These external electrodes consisted of textile bands with a width of 3 cm (used for arms) or 4 cm (used for lower legs) and were made of conductive fabric. The electrodes on the non-dominant limb were connected to a HF voltage generator (i.e., an arbitrary waveform generator (4065 from B&K Precision, Yorba Linda, CA, US) connected to a custom-made class AB amplifier). Sinusoidal voltage bursts (carrier frequency of 6.78 MHz and  $FB = 0.1$ ; where  $F = 1$  kHz is the repetition frequency of the bursts and  $B = 100 \mu s$  is their duration) of different amplitudes (increasing order) were applied to check if the participant perceived some discomfort. Once the preliminary assay was performed (without any notification of sensations by any of the participants), a pair of intramuscular needle electrodes were inserted either into the brachial biceps or into the medial gastrocnemius of the non-dominant limb for the arm and lower leg respectively, under aseptic conditions. These needle electrodes had a diameter of 0.4 mm and a length of 20 mm of which only the distal 17.5 mm were inserted (i.e., an implantation depth of 17.5 mm). The needle has a 3 mm long exposed surface on its tip (530607 from Inomed Medizintechnik GmbH, Emmendingen, Germany; see inset Fig. 1b). The needle electrodes were connected to a discrete potentiometer (3683S-1-202L from Bourns Inc., Riverside, CA, US) using short cables (maximum of 12 cm) to avoid inductive and capacitive wiring effects. After that, the remaining assays (i.e., maximum transferable power, powering electronic devices, and temperature evolution in 18 minutes, these last two assays being reported in supplementary material) were conducted. Once the last assay was finished, the textile electrodes were unstrapped, the needle electrodes were extracted and the skin areas where the electrodes had been located were inspected. No damage was observed in these areas or in the electrodes. Only one case (arm of P2) presented small-sized superficial hematomas in the areas where the needle electrodes had been inserted approximately one hour after the extraction. The temperature of the limb was monitored using a thermal imaging infrared camera (E60 from FLIR Systems Ltd, Wilsonville, OR, US) during the entire phase. The second phase was repeated for the other limb. The order of the limbs was randomized among the participants.

### C. MRI Acquisition and Segmentation

Each participant underwent MRI images acquisition, recording four sequences per limb: T1 axial (slice resolution =  $0.52 \times 0.52$  mm; slice thickness = 6 mm), T1 sagittal (slice resolution =  $1.04 \times 1.04$  mm; slice thickness = 4.8 mm), T1 coronal (slice resolution =  $1.04 \times 1.04$  mm; slice thickness = 4.65 mm), and T2 axial (slice resolution =  $0.52 \times 0.52$  mm; slice thickness = 6 mm). These sequences were acquired with a 3 Tesla system (Magnetom Trio, a Tim System from Siemens Healthcare GmbH, Erlangen, Germany). Four different tissues were segmented: 1) bone, which included cortical and trabecular tissues, bone marrow, and articular cartilages (e.g., meniscus), 2) muscle, including tendons, ligaments, and intramuscular fat, 3) subcutaneous fat, and 4) skin. For the segmentation of bone, muscle and fat, the procedure started by manually segmenting the T1 axial acquisition every other slice. The initial segmentation of the skin had to be performed using a different procedure since it was not visible in the entire MRI stack because of its thinness. The skin thickness was approximated by measuring it in different slices of the MRI, and then the skin was generated by performing a 2D axial dilation on the fat segmentation. The measured skin thicknesses are reported in Table I. For each tissue, the remaining slices were interpolated with the “3D interpolation” built-in tool of The Medical Imaging Interaction Toolkit from the German Cancer Research Center, Heidelberg, Germany. This interpolation was based on the radial basis function interpolation [53] and on Laplacian smoothing [54]. Minor manual adjustments were required to correct sharp curvatures of the geometry in the interpolated slices. Finally, smoothed surface meshes were generated from the 3D interpolation (see Fig. 2) and then exported for numerical computation. The MRI fiducial markers centers (three for each band electrode and one for each needle electrode) were precisely annotated.

TABLE I  
MEASURED SKIN THICKNESS FROM MRI IMAGES FOR EACH PARTICIPANT AND LIMB

| Skin thickness (mm) | P1   | P2   | P3   | P4   | P5   |
|---------------------|------|------|------|------|------|
| Arm                 | 1.75 | 1.50 | 1.50 | 2.00 | 1.75 |
| Lower leg           | 1.50 | 2.00 | 1.75 | 2.00 | 2.25 |

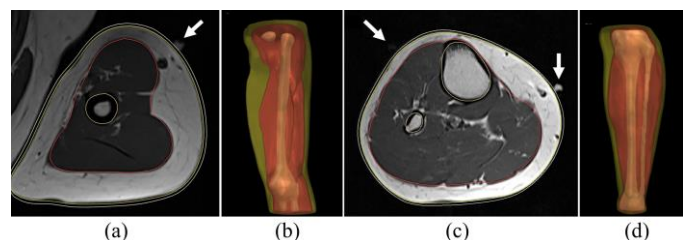


Fig. 2. Examples of smoothed surface meshes and markers position from MRI images. White arrows indicate the MRI markers for electrode placement. (a) Axial slice of arm. (b) 3D representation of segmented arm. (c) Axial slice of lower leg. (d) 3D representation of segmented lower leg. Bone mesh in brown, muscle in red, fat in yellow, and skin in white (only in (a) and (c)).

### D. Assay for Measuring the Maximum Transferable Power

The maximum received power for an optimal resistive load was obtained. For that, first, sinusoidal voltage bursts (carrier

frequency of 6.78 MHz and  $FB = 0.1$  ( $F = 1$  kHz)) were applied across the external electrodes and the optimal load (i.e., the resistance that provides maximum power transfer) was experimentally found by adjusting the resistance of the discrete potentiometer. Then, with the optimal load connected to the intramuscular electrodes and the same voltage waveform applied across the external electrodes, different amplitudes were applied. The externally applied voltage amplitude, the external current amplitude, together with the voltage amplitude at the load ( $V_{\text{load}}$ ) were measured (Fig. 3). For each amplitude, the received power at the load or power delivered to the load (PDL) was computed as

$$P_{\text{load}} = \frac{V_{\text{load RMS}}^2}{R_{\text{load}}} = \frac{V_{\text{load}}^2}{R_{\text{load}}} k^2 FB, \quad (1)$$

where  $R_{\text{load}}$  is the optimal load and the scaling factor  $k\sqrt{FB}$ , with  $k = \sqrt{11/32}$ , transforms amplitude values into RMS values for the applied waveform (see supplementary material Section SA for details of the applied waveform). The average channel efficiency or power transmission efficiency (PTE) was also computed as the ratio between the received power ( $P_{\text{load}}$ ) and the externally applied power ( $P_{\text{total}}$ ):

$$PTE = \frac{P_{\text{load}}}{P_{\text{total}}} \cdot 100. \quad (2)$$

#### E. Perception of Heat-Related and Electrical-Stimulation-Related Sensations

During the second phase of the experimental procedures, self-perception of heat-related (HR) and electrical-stimulation-related (ESR) sensations was monitored. In particular, the participants were asked for oral notification of any HR or ESR sensation at any time without knowing when the HF voltage bursts were applied. In case of sensation, the HR perception was classified into three intensity levels (1-Not sure, 2-Pleasant warmth and 3-Unpleasant warmth) and the ESR perception was classified into three intensity levels (1-Not sure, 2-Pleasant sensation and 3-Unpleasant sensation) and five categories (1-Tingling, 2-Puncture, 3-Pressure, 4-Pain and 5-Other).

#### F. Electrical Safety

Safety standards for human exposure to electromagnetic fields [47], [48] identify two general sources of risk regarding passage of alternating currents through the body which limit the amplitude of the currents that can be applied: 1) risks caused by unsought electrical stimulation of excitatory tissues and 2) risk of thermal damage due to Joule heating. Risks caused by unsought stimulation can be avoided if the frequency of the applied currents is high enough. In particular, the standard followed in the present study (the IEEE standard [48]) determines that, for continuous sinusoidal currents with a frequency above 5 MHz, electrostimulation is not a matter of concern. The electrostimulation risks are especially relevant for low frequencies ( $< 100$  kHz). However,

if the sinusoidal currents are applied in the form of bursts, the generated low frequency harmonics must be considered [22]. In this study, sinusoidal voltage bursts (carrier frequency of 6.78 MHz and  $FB = 0.1$  ( $F = 1$  kHz)) were applied. To minimize the contribution of the generated low frequency harmonics, the applied bursts were smoothed with a tapered cosine window (with  $r = 0.5$ , see supplementary material Section SA for details of the applied waveform). Applying the expression for non-sinusoidal fields established in the safety standard to the used voltage waveform, the maximum peak electric field that can be applied (i.e., the maximum *in situ* electric field to avoid electrostimulation) is above 200 MV/m (see supplementary material Section SB). This limit is far above the electric field amplitudes that were computed to be produced during the experimental sessions. Risk of thermal damage due to Joule heating is addressed by the standards by imposing a limitation to the so-called specific absorption rate (SAR) which has units of W/kg and indicates the heat dissipated per unit of tissue mass due to Joule heating. In the case of limbs, the IEEE standard indicates that the maximum admissible SAR is 20 W/kg, space-averaged over any cubical 10-g of tissue and time-averaged for 6 minutes. In order to ensure that the SAR restriction was met during the experimentation, the external voltages were applied for short time exposures (i.e.,  $< 30$  seconds). On the other hand, the SAR values indicated in Section III.A correspond to projected SAR values for exposures longer than 6 minutes. That is, the electric field magnitudes obtained with the 3D computational models (see Section II.H) were used to compute the SAR that would be produced by sinusoidal voltage bursts continuously applied for 6 minutes or more. The IEEE standard indicates another limit with respect to the whole-body SAR averaged for 1 hour. In all cases, the projected whole-body SAR was below this limit (i.e., 0.4 W/kg) for exposures longer than 1 hour.

#### G. Measurement Apparatus

The electrical ac measurements were acquired using a floating digital oscilloscope (TPS2014 from Tektronix, Inc., Beaverton, OR, US). For the applied external voltage and the potentiometer voltage, active differential probes (TA043 from Pico Technology Ltd, Saint Neots, UK) were used. A current probe (TCP2020A from Tektronix, Inc., Beaverton, OR, US) was used for the applied external current (i.e., current corresponding to the applied external voltage). This is shown in Fig. 3.

#### H. Numerical Methods

The segmented meshes obtained from the MRI images of the tissues were imported into COMSOL Multiphysics 5.3 (from COMSOL, Inc., Burlington, MA, US) to create the 3D computational model. To numerically determine the electric field and voltage distributions inside the tissues, the “electric current” physics that is included inside the ac/dc module of COMSOL was used. The geometry of each one of the ten studied 3D computational models consisted in a four-tissue layered segmented limb obtained from the MRI images.



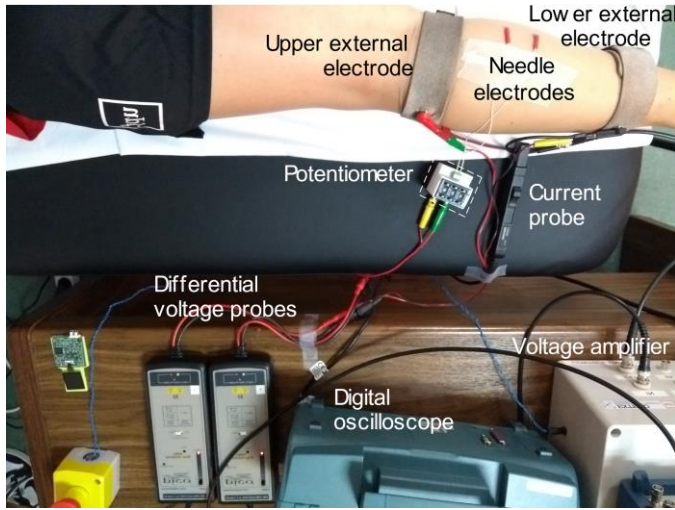


Fig. 3. Experimental ac measurement setup.

The four layers, from the most peripheral to the most internal one, were: skin, fat, muscle, and cancellous bone. The passive electrical properties and densities of the tissues are reported in Table II. Two cylindrical electrodes with a diameter of 0.4 mm, and a total length of 20 mm emulated the needle electrodes that we used in the experimental part. Their length was divided into two longitudinal sections: 17 mm of insulating material and 3 mm of exposed surface at the tip of the needle. The position of these electrodes was determined using the coordinates of the MRI markers. They were perpendicularly aligned with the skin tissue and were inserted 17.5 mm inside the tissues. The position coordinates of the external electrodes were also identified in the MRI using three markers per electrode. These data were used to obtain a three-point plane. Following, a plane parallel to the previous one was created with a separation distance of 30 mm for the arms and 40 mm for the lower legs (i.e., the width of the band electrodes used during the experimentation). Then, the superficial tissue area encompassed between both planes was considered the area of the external electrodes. Finally, the whole limb was set inside a block that emulated the air. The size of this block was adjusted for each case to guarantee a minimum of 2 cm gap of air in any direction. The density and electrical properties of non-biological materials are reported in Table III. Fig. 4 shows the resultant geometry of the 3D computational model of the arm of participant P4.

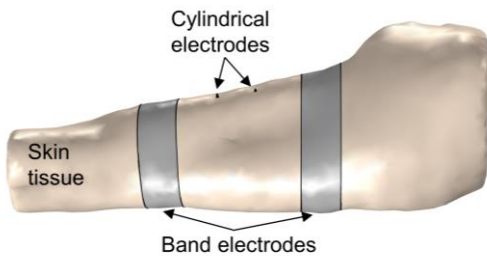


Fig. 4. Geometry of the 3D computational model (COMSOL) of the arm of P4. The air box that surrounded the arm has been intentionally hidden for visualization purposes.

TABLE II  
PASSIVE ELECTRICAL PROPERTIES AND DENSITY OF MODELED TISSUES AT A  
FREQUENCY OF 6.78 MHz [55]

| Dielectric properties @ 6.78MHz | Conductivity (S/m) | Relative permittivity | Density (kg/m <sup>3</sup> ) |
|---------------------------------|--------------------|-----------------------|------------------------------|
| Skin                            | 0.147              | 478                   | 1109                         |
| Fat (subcutaneous)              | 0.0496             | 35                    | 911                          |
| Muscle                          | 0.602              | 233                   | 1090                         |
| Bone (cancellous)               | 0.116              | 90                    | 1178                         |

TABLE III  
ELECTRICAL PROPERTIES OF NON-BIOLOGICAL MATERIALS

| Dielectric properties                            | Conductivity (S/m) | Relative permittivity | Density (kg/m <sup>3</sup> ) |
|--|--------------------|-----------------------|------------------------------|
| Conductive electrodes (Steel, 0.65% carbon) [56] | $5.5 \cdot 10^6$   | 1                     | 7844                         |
| Insulating material of needle electrodes [57]    | $1 \cdot 10^{-17}$ | 3.2                   | 1000                         |
| Air (at 20°)                                     | $1 \cdot 10^{-9}$  | 1                     | 1.2                          |

The electrical coupling between the external electrodes and the needle electrodes was modeled as a two-port network. This model included the external electrodes, the limb tissues, and the needle electrodes (emulated as cylinders). Since all its elements were passive, the system could be considered reciprocal [58]. Therefore, voltages and currents at the network could be expressed as

$$\begin{pmatrix} V_{\text{ext}} \\ V_{\text{int}} \end{pmatrix} = \begin{pmatrix} Z_{\text{ext}} & Z_{12} \\ Z_{12} & Z_{\text{int}} \end{pmatrix} \begin{pmatrix} I_{\text{ext}} \\ I_{\text{int}} \end{pmatrix}, \quad (3)$$

where  $V_{\text{ext}}$  is the voltage across the external electrodes,  $V_{\text{int}}$  is the voltage across the needle electrodes,  $I_{\text{ext}}$  is the current through the two external electrodes and  $I_{\text{int}}$  is the current through the needle electrodes. By definition,

$$Z_{\text{ext}} \stackrel{\text{def}}{=} \left. \frac{V_{\text{ext}}}{I_{\text{ext}}} \right|_{I_{\text{int}}=0}, \quad Z_{\text{int}} \stackrel{\text{def}}{=} \left. \frac{V_{\text{int}}}{I_{\text{int}}} \right|_{I_{\text{ext}}=0}, \quad Z_{12} \stackrel{\text{def}}{=} \left. \frac{V_{\text{int}}}{I_{\text{ext}}} \right|_{I_{\text{int}}=0} = \left. \frac{V_{\text{ext}}}{I_{\text{int}}} \right|_{I_{\text{ext}}=0}. \quad (4)$$

The impedances  $Z_{\text{ext}}$  and  $Z_{12}$  were determined by simulating the delivery of a reference current (1 A at 6.78 MHz) through the external electrodes, while keeping  $I_{\text{int}}$  equal to 0, and measuring the voltage across the external electrodes (for  $Z_{\text{ext}}$ ) and the voltage across the needle electrodes (for  $Z_{12}$ ). The same procedure was done for determining  $Z_{\text{int}}$  but, in this case, applying a reference current through the needle electrodes and measuring the voltage across the needle electrodes.

The parameters obtained for the five participants are summarized in Tables IV and V, for the arm and the lower leg respectively. Note that the impedance parameters  $Z_{\text{int}}$  and  $Z_{12}$  include three different angles ( $0^\circ$ ,  $-10^\circ$ ,  $+10^\circ$ ). As the needle electrodes were inserted manually, a misalignment of  $\pm 10^\circ$  between both electrodes could be obtained (see inset in Fig. 7a). An alignment of  $0^\circ$  corresponds to a parallel alignment between both cylindrical electrodes,  $-10^\circ$  corresponds to the case when the distance between both tip electrodes was minimum and  $+10^\circ$  corresponds to the case when the separation distance on the tips was maximum.

TABLE IV  
ARM IMPEDANCE PARAMETERS AT 6.78 MHZ

| Impedances                | P1     | P2      | P3      | P4        | P5        |
|---------------------------|--------|---------|---------|-----------|-----------|
| $Z_{\text{ext}} (\Omega)$ | 94-29i | 95-28i  | 104-32i | 59-15i    | 56-19i    |
| $Z_{\text{int}} (\Omega)$ | 0°     | 423-63i | 460-69i | 432-65i   | 450-62i   |
|                           | -10°   | 418-62i | 454-68i | 424-63i   | 411-61i   |
|                           | +10°   | 430-64i | 484-73i | 444-67i   | 431-64i   |
| $Z_{12} (\Omega)$         | 0°     | 19-4i   | 20-4i   | 19-4i     | 13-2.3i   |
|                           | -10°   | 15-3.1i | 17-3.4i | 14-7.3i   | 8.1-1.5i  |
|                           | +10°   | 22-4.6i | 23-4.7i | 23-4.9i   | 17.8-3.2i |
|                           |        |         |         | 15.8-3.8i |           |

TABLE V  
LOWER LEG IMPEDANCE PARAMETERS AT 6.78 MHZ

| Impedances                | P1     | P2       | P3       | P4       | P5       |
|---------------------------|--------|----------|----------|----------|----------|
| $Z_{\text{ext}} (\Omega)$ | 79-19i | 72-20.1i | 87-24i   | 60-15.1i | 61-15.5i |
| $Z_{\text{int}} (\Omega)$ | 0°     | 429-63i  | 423-63i  | 491-73i  | 419-62i  |
|                           | -10°   | 425-63i  | 420-62i  | 484-72i  | 419-62i  |
|                           | +10°   | 438-65i  | 428-63i  | 547-83i  | 410-60i  |
| $Z_{12} (\Omega)$         | 0°     | 7.6-1.3i | 7.7-1.3i | 6.7-1.2i | 7.6-1.3i |
|                           | -10°   | 6.4-1.1i | 6.3-1.1i | 5.5-1i   | 6.1-1.1i |
|                           | +10°   | 8.9-1.5i | 9.1-1.6i | 8-1.4i   | 9.3-1.6i |
|                           |        |          |          | 8.9-1.6i |          |

Modelling the z-parameters as a T-circuit, the PDL can be expressed as

$$P_{\text{load}} = |I_{\text{load}}|^2 \Re(Z_{\text{load}}), \quad (5)$$

where  $P_{\text{load}}$  is the power dissipated at the load, and  $I_{\text{load}}$  is the current flowing through the load.  $I_{\text{load}}$  can be calculated as

$$I_{\text{load}} = I_{\text{ext}} \frac{Z_{12}}{Z_{\text{int}} + Z_{\text{load}}}, \quad (6)$$

being  $I_{\text{ext}}$  the current applied through the external electrodes. The PTE of the system is calculated using (2). In addition, the 3D computational model was also used to calculate the electric potential and the electric field magnitude distributions inside the tissues. For that, a sinusoidal voltage (frequency = 6.78 MHz) was applied to the external electrodes, being its RMS value equal to the RMS value of the experimental applied waveform. The transformation from amplitude values into RMS values was done by applying the mentioned scaling factor  $k\sqrt{FB}$ , with  $k = \sqrt{11/32}$ . The projected local SAR was calculated from the electric field magnitude according to the safety standard, with equation

$$\text{SAR} = \frac{\sigma |E_{\text{rms}}|^2}{\rho}, \quad (7)$$

where  $\sigma$  is the local tissue conductivity,  $\rho$  is the local tissue density and  $E_{\text{rms}}$  is the RMS value of the computed electric field. The SAR was space-averaged over any cubical 10 g of tissue following the guidelines of the standard [48], [59].

### III. RESULTS

#### A. Maximum Transferred Power

Fig. 5a shows an MRI image corresponding to the arm of participant P3. The markers of the external electrodes can be observed in this image. After building a 3D computational

model from the MRI images, the electric field, the electric potential and the projected SAR (see definition in Section II.F) distributions were numerically calculated. It can be observed that, within the region encompassed by the two external electrodes, a few millimeters away from them, the electric field is coarsely uniform where the section of the limb smoothly changes (arm of the participant P3: Fig. 5b, rest of limbs: supplementary material Fig. S4). Consequently, the electric potential coarsely drops linearly between those electrodes (arm of the participant P3: Fig. 5c, rest of limbs: supplementary material Fig. S5). Regarding the projected SAR distribution, it can be noted that maxima are generally located near the external electrodes. However, it is also worth noting that the values of these SAR maxima do not differ substantially from the SAR values where the needle electrodes were placed (arm of the participant P3: Fig. 5d, rest of limbs: supplementary material Fig. S6). Thus, the fact of having the SAR maxima close to the external electrodes does not significantly limit the maximum power transferred to the implants.

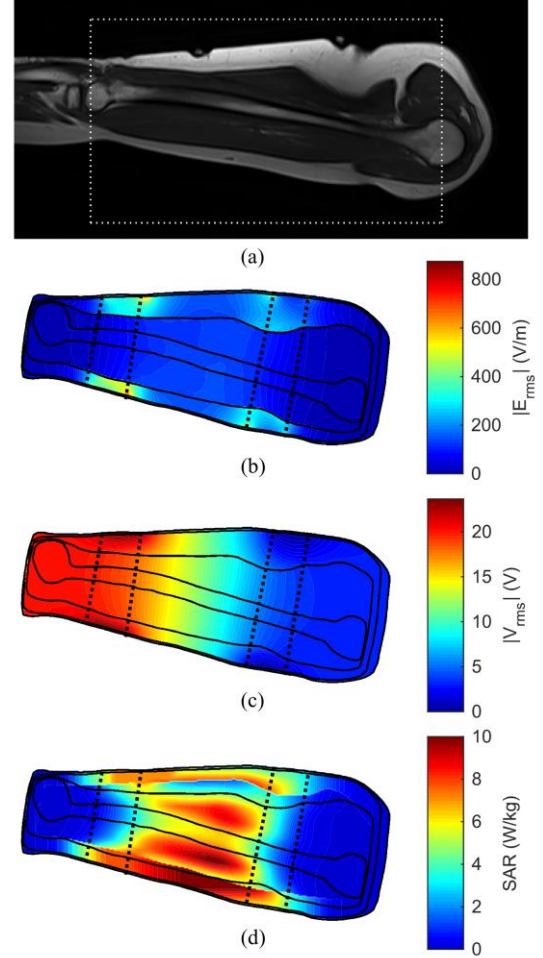


Fig. 5. Examples of MRI, computed electric field, electric potential and projected SAR distributions, and power transfer experimental results. Black dashed lines indicate the positions of the external electrodes. (a) MRI image of the arm of participant P3 (i.e., A3), b-d were computed inside the white-dashed box of the same participant. (b) Computed electric field distribution. (c) Computed electric potential distribution. (d) Computed projected SAR distribution.

The average optimal load (i.e., the resistance that experimentally maximized the received ac power) was  $(244 \pm 9) \Omega$  (mean  $\pm$  standard error of the mean, SEM) for the arms and  $(258 \pm 6) \Omega$  (mean  $\pm$  SEM) for the lower legs (see Table VI).

TABLE VI  
OPTIMAL  $Z_{\text{LOAD}}$  FOR EACH PARTICIPANT AND LIMB

| $Z_{\text{load}} (\Omega)$ | P1  | P2  | P3  | P4  | P5  |
|----------------------------|-----|-----|-----|-----|-----|
| Arm                        | 210 | 250 | 260 | 250 | 250 |
| Lower leg                  | 260 | 250 | 280 | 250 | 250 |

The received ac powers or PDL (for the optimal load) for both limbs of all the participants are reported in Fig. 6a. This time-averaged power was obtained in the load with it connected to the pair of intramuscular electrodes when sinusoidal voltage bursts (carrier frequency = 6.78 MHz,  $FB = 0.1$  ( $F = 1$  kHz)) were applied across the external electrodes. It can be observed that the received ac power shows a quadratic dependency on the externally applied voltage amplitude.

Powers up to a projected maximum SAR of 20 W/kg, which is the limit imposed by the IEEE safety standard [48] for limbs in controlled settings, are reported for arms of P2 and P5. In the remaining cases, the maximum reported power corresponds to a lower projected SAR due to technical limitations (i.e., maximum output amplitude of the generator) during the experimentation. For the arms, the maximum received power ranges from 7.7 mW (A4) to 13.7 mW (A2), with an average value of  $(10 \pm 2)$  mW (mean  $\pm$  SEM). For the lower legs, these values are noticeably lower. They range from 3.1 mW (LL1) to 6.1 mW (LL5), with an average value of  $(4.3 \pm 0.6)$  mW (mean  $\pm$  SEM). These results indicate that powers in the order of milliwatts can be transferred while complying with the safety standard. For a projected maximum SAR of 10 W/kg, the received powers in the arms range from 4.0 mW (A5) to 7.3 mW (A3), with an average value of  $(5.9 \pm 0.7)$  mW (mean  $\pm$  SEM), and in the lower legs they range from 2.0 mW (LL1) to 3.3 mW (LL5), with an average value of  $(2.4 \pm 0.3)$  mW (mean  $\pm$  SEM) (see Fig. 6b).

The channel efficiency, or PTE, for every single case is reported in Fig. 6c. For the arms, it ranges from 0.15% (A4) to 0.27% (A2), with an average value of  $(0.19 \pm 0.03)\%$  (mean  $\pm$  SEM). For the lower legs, it ranges from 0.029% (LL3) to 0.047% (LL5), with an average value of  $(0.035 \pm 0.003)\%$  (mean  $\pm$  SEM). The difference between arms and lower legs is mainly due to the anatomical characteristics of both limbs (e.g., volume, section, length, fat thickness, etc.) [48]. These power transfer efficiencies in the order of 0.1% are much lower than those typically reported, in the order of 1% or even in the order of 10%, for WPT systems based on inductive coupling or ultrasonic acoustic coupling [27], [60].

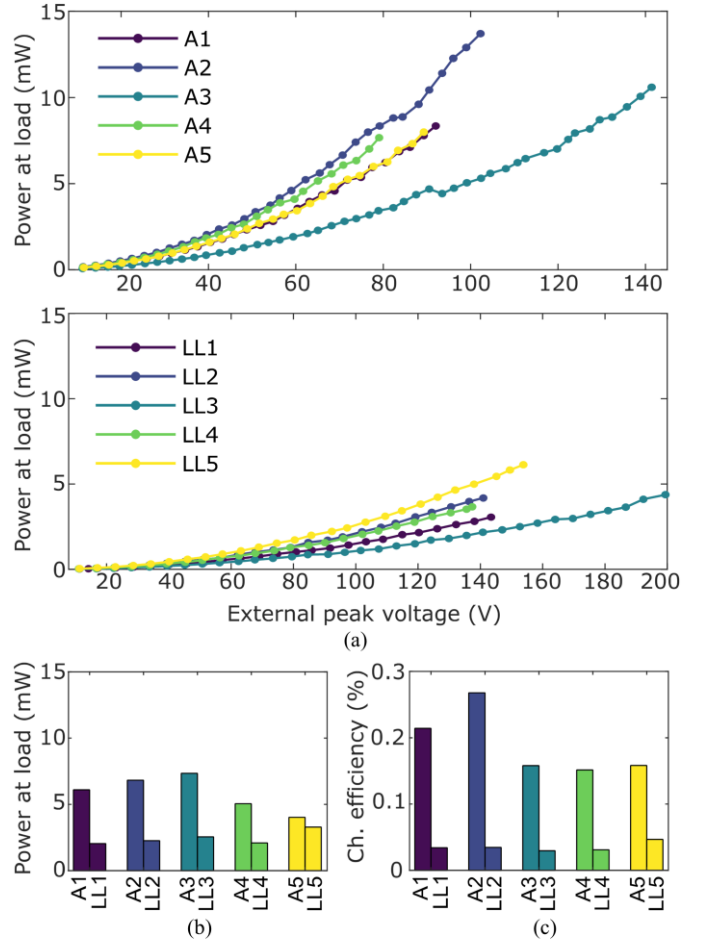


Fig. 6. (a) Maximum transferred power to the optimal load (or PDL) connected across the pair of intramuscular needle electrodes when sinusoidal voltage bursts (carrier frequency = 6.78 MHz, and  $FB = 0.1$  ( $F = 1$  kHz)) were applied across the pair of external electrodes: in the arms (i.e., A1 to A5) on top and in the lower legs (i.e., LL1 to LL5) on the bottom. Dots indicate experimental measurements. (b) Maximum transferred power to the optimal load with a projected maximum SAR of 10 W/kg. (c) Channel efficiency or PTE.

### B. Experimental Measurements versus Computational Model

The transmission channel formed by the band electrodes, the tissues and the needle electrodes was modeled as a two-port impedance network (Fig. 7a) [50]. The impedance ( $Z$ ) parameters of the network were numerically computed using the 3D computational model of the limb obtained after segmenting the MRI images. The obtained two-port impedance networks allow simulating power transfer with reasonable accuracy. As an example, when applying a peak voltage of 79 V across the external electrodes, the average relative error between the experimentally received power and the simulated one is 4%, with a standard deviation of 26% (see Fig. 7b-f).



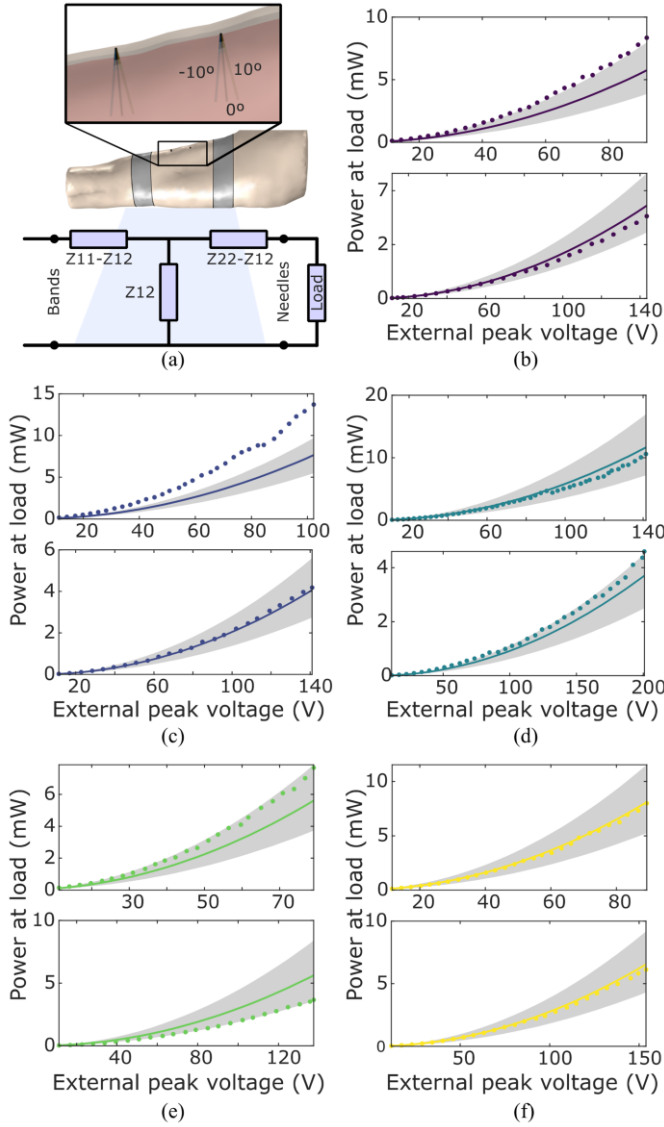


Fig. 7. Computational modeling results. (a) The transmission channel (i.e., limb tissues, band electrodes and needle electrodes) was modeled as a two-port network. The inset shows the considered insertion angle error of the needle electrodes. (b) Comparison of experimental maximum transferred power and simulated transferred power using the optimal experimental load in the arm (top) and in the lower leg (bottom) of P1. Dots indicate experimental measures. Solid line indicates simulated results under the assumption that both needle electrodes are perfectly aligned (i.e.,  $0^\circ$ ). Upper shadow edge indicates simulated results under the assumption that both needle electrodes have an inclination of  $-10^\circ$  (i.e.,  $10^\circ$  towards the center). Lower shadow edge indicates simulated results under the assumption that both needle electrodes have an inclination of  $+10^\circ$  (i.e.,  $10^\circ$  towards the band electrodes). (c) Same as Fig. 7b for P2. (d) Same as Fig. 7b for P3. (e) Same as Fig. 7b for P4. (f) Same as Fig. 7b for P5.

#### IV. DISCUSSION

The obtained results highlight that the electric potential within the tissues located between the external electrodes coarsely drops linearly (Fig. 5b-c). This is noteworthy for two reasons: 1) the electric field at the location of an implant (and hence the power obtained by the implant [22]) would not depend on the implantation depth, and 2) WPT based on volume conduction can be considered to be a non-focused WPT method since the applied electric field is present in the whole inter-electrode region. Examples of non-focused

methods are those based on Helmholtz-like coil configurations [61]. Non-focality implies that WPT based on volume conduction can be used for powering multiple implants with the same external energy source (this fact is illustrated in supplementary material Section SC). Moreover, each device only draws a small portion of the total external energy without significantly distorting the electric field at the location of the other implant, thus enabling the possibility of increasing the total efficiency of the method by increasing the number of devices in the same powered area [51].

For safety and practical reasons, some relevant parameters that may affect the PDL and the PTE such as the number of implants (i.e., pairs of needle electrodes), their relative and absolute position, the distance between the needle electrodes or their depth were not studied. However, we analyzed these parameters in previous works using analytical approaches [22] and simplified computational models [51].

Table VII contains a comparison of the most representative WPT methods for implants. Proposals based on volume conduction (VC), ultrasonic acoustic coupling (US), mid-field coupling (MF), and near-field inductive coupling (IC) are included. In general, VC is less efficient than other methods such as US or IC. Indeed, the proposed approach is very poor in terms of PTE if a single implant is powered as most of the power is lost in the form of Joule heating in the tissues. It can be stated that our approach sacrifices power efficiency for minimal invasiveness. However, the PTE increases if multiple implants are simultaneously supplied as the externally applied power will be the same [51]. PTE also increases as the distance between the implant electrodes increases [22]. The low PTE of VC does not jeopardize the feasibility of using a wearable external system (such as the one showed in the envisioned scenario in Fig. 1a). Considering the average PTE (i.e., 0.19% and 0.035% for arms and lower legs, respectively) and the power consumption of electronic medical implants (typically 1 mW or less), the externally applied power should be in the order of 0.5 and 3 W for the arms and lower legs, respectively. There are several wearable rechargeable batteries (e.g., 100 cm<sup>3</sup> or less) in the market that provide more than 30 W for one hour (e.g., 2447-3034-20-520 from Ansmann AG, Assamstadt, Germany). In terms of PDL, VC is generally superior (on tissue). However, comparison in terms of PTE and PDL with published WPT systems is not straightforward as PTE and PDL depend on multiple factors such as the geometry of the elements (e.g., the dimensions of the external applicator and of the implants) and the relative conformation of the elements of the system (e.g., whether the implants are within a region encompassed by the applicator of the transmitter or the implantation depth). In fact, for some conformations, volume conduction is advocated by some researchers because of its superior efficiency [26]. The geometry, dimensions, and implantation depth of the harvester component (i.e., the implant) not only affect the PTE and PDL, but also the viability of the method. Depending on the clinical application, there are geometries that are more appropriate as well as maximum/minimum dimensions and/or implantation depths. To consider these factors, Table VII

contains four figures of merit. Figure of Merit 1 (FoM<sub>1</sub>) has been determined as the ratio of the PDL to the maximum dimension. Figure of Merit 2 (FoM<sub>2</sub>) has been determined as the ratio of the PDL to the second maximum dimension. Figure of Merit 3 (FoM<sub>3</sub>) highlights the potential of the method to transfer powers when implants are deeply placed. It is calculated as the PDL multiplied by the square of the depth. Finally, Figure of Merit 4 (FoM<sub>4</sub>) is the volumetric power density of the harvester component. It is calculated as the ratio of the PDL to the harvester volume. Although our method presents a low PDL to maximum dimension ratio (FoM<sub>1</sub> = 0.19 mW/mm), it is superior in terms of PDL to the second maximum dimension ratio (FoM<sub>2</sub> = 14.3 mW/mm) and of the volumetric power density (FoM<sub>4</sub> = 7.6 mW/mm<sup>3</sup>). All this suggests that our method is a suitable approach for elongated flexible threadlike devices that can be easily deployed by injection and powered by wearable external units. In addition, it has a good score in terms of depth capability (FoM<sub>3</sub> = 17.4 mWcm<sup>2</sup>), suggesting that the devices could be placed at implantation depths in the order of few centimeters. In any case, these comparisons must be considered as inconclusive because the compared proposals have been validated by using different media and/or SAR references. For example, our work is the only one validated in human volunteers. Further research is required regarding this aspect.

Regarding the two-port model, after analyzing the impact of different possible sources of error in the experimental procedures and in the simulations, it was determined that the variability in the insertion angle of the needle electrodes was the most likely cause of the discrepancies observed between the simulated and the experimental results. This variability

causes significant random errors in the separation distance between the conductive tips of the electrodes. Even though the location of the insertion point of the needles was carefully ensured by using markers, the insertion was performed manually orthogonally to the skin without any provision to ensure the penetration angle. Simulations were performed assuming  $\pm 10^\circ$  errors in the penetration angle. Considering this penetration angle error margin, the simulations fit the experimental results in all cases except for the arm of P2. This inconsistency may be caused by the fact that, in this case, the insertion marks of the needle electrodes had to be displaced 5 mm from the original position to avoid a blood vessel that was detected in the MRI images. Although the position of the needles was accordingly modified on the numerical model, this adjustment may explain the inconsistency.

None of the participants reported any sensation related to heat or electrostimulation during the experimentation in both limbs. They barely reported uncomfortable sensations related to the fact of having the needles inserted. Therefore, the applied HF current bursts are not only innocuous, as guaranteed by adherence to the IEEE standard, but also imperceptible. No skin alterations were observable. This study focuses on the safety of the method by following the IEEE standard on safety levels with respect to human exposure to electromagnetic fields. These aspects can be extrapolated to chronic implants but, for the final application (chronic use with implantable devices), there are other safety aspects (e.g., long-term electrode changes, mechanical stability, etc.) that should be analyzed in chronic animal studies.

TABLE VII  
COMPARISON OF THE MOST REPRESENTATIVE WPT METHODS FOR IMPLANTS

| Parameter                              | This work    | [17]                  | [23]          | [62]       | [63]                  | [64]                  | [14]                  | [65]                  | [66]                  | [67]  | [68]                  | [69]          |
|--|--------------|-----------------------|---------------|------------|-----------------------|-----------------------|-----------------------|-----------------------|-----------------------|-------|-----------------------|---------------|
| WPT method                             | VC           | VC                    | VC            | US         | US                    | MF                    | MF                    | MF                    | IC                    | IC    | IC                    | IC            |
| Medium                                 | Human tissue | <i>Ex vivo</i> tissue | NaCl solution | Castor oil | <i>In vivo</i> tissue | <i>In vivo</i> tissue | <i>In vivo</i> tissue | <i>Ex vivo</i> tissue | <i>Ex vivo</i> tissue | Air   | <i>In vivo</i> tissue | NaCl solution |
| Depth (cm)                             | 1.75         | 0.25                  | 2.75          | 3          | 2.15                  | 4                     | 4                     | 5                     | 1.2                   | 2     | 2.5                   | 5             |
| Volume (mm <sup>3</sup> )              | 0.75*        | 1600                  | 314           | 1.1        | 0.42                  | 5.3                   | ~6.3                  | 38                    | 0.79                  | ~950  | ~0.13                 | 1150          |
| Max. dimension (mm)                    | 30**         | 28.3                  | 20            | 1.2        | 1.1                   | 3.4                   | 2                     | 7.5                   | 1.4                   | 22    | 1                     | 30            |
| 2 <sup>nd</sup> Max. dimension (mm)    | 0.4          | 20                    | 20            | 1.2        | 0.9                   | 1.5                   | 2                     | 5.6                   | 1.4                   | 22    | 0.5                   | 9             |
| SAR (W/kg)                             | 10           | 2                     | 2             | †          | †                     | 8.9                   | 10                    | -                     | 1.6                   | -     | 1.6                   | 2             |
| PDL (mW)                               | 5.7          | 137.8                 | 10            | 2.1        | 0.35                  | 0.6                   | 2.2                   | 6.7                   | 0.22                  | 80    | 0.036                 | 10            |
| P <sub>Total</sub> (W)                 | 2.85         | 0.25                  | 2.2           | 0.08       | -                     | 0.8                   | 0.5                   | 1                     | 0.04                  | 0.4   | -                     | 2.5           |
| PTE (%)                                | 0.2          | 55.1                  | 0.5           | 2.6        | -                     | 0.1                   | 0.4                   | 0.7                   | 0.6                   | 20    | -                     | 0.4           |
| FoM <sub>1</sub> (mW/mm)               | 0.19         | 4.87                  | 0.5           | 1.75       | 0.32                  | 0.18                  | 1.1                   | 0.9                   | 0.16                  | 4.55  | 0.22                  | 0.33          |
| FoM <sub>2</sub> (mW/mm)               | 14.3         | 6.9                   | 0.5           | 1.8        | 0.4                   | 0.4                   | 1.1                   | 1.2                   | 0.2                   | 3.6   | 0.1                   | 1.1           |
| FoM <sub>3</sub> (mWcm <sup>2</sup> )  | 17.4         | 8.6                   | 75.6          | 18.9       | 1.6                   | 9.6                   | 35.2                  | 167.5                 | 0.3                   | 320   | 0.036                 | 250           |
| FoM <sub>4</sub> (mW/mm <sup>3</sup> ) | 7.6          | 0.086                 | 0.032         | 1.91       | 0.83                  | 0.11                  | 0.35                  | 0.18                  | 0.28                  | 0.084 | 0.28                  | 0.01          |

†The used acoustic intensity was 720 mW/cm<sup>2</sup>. \*Volume of the intramuscular electrodes (diameter = 0.4 mm, length: 3 mm). \*\*Inter electrode spacing.

## V. CONCLUSIONS

This study in healthy participants demonstrates that, albeit with poor efficiency, ac and dc electric powers in the order of

milliwatts can be obtained from pairs of thin electrodes within limb muscles when HF sinusoidal current bursts are safely delivered through two textile electrodes shaped as bands strapped around the limb and encompassing the region where

the pair of thin electrodes is located. In addition, it is demonstrated that these currents are imperceptible and that the obtained power from the pair of thin electrodes can be used to power complex electronic circuits with digital and analog functionalities (this fact is illustrated in supplementary material Section SC).

In addition to unprecedented minimal invasiveness, other remarkable advantages of the presented approach over other WPT methods are the capabilities to: 1) power deep implants, 2) simultaneously power multiple implants with the same external applicator, 3) deliver high peak powers and 4) avoid inconvenient external applicators and elements such as rigid bulky coils for inductive coupling or gels for ultrasonic acoustic coupling.

To the best of our knowledge, this is the first time that the use of WPT based on HF volume conduction has been validated in humans with a focus on implantable devices. Previous studies were performed *in silico*, *in vivo* or *ex vivo* but never in humans. This is significant because the tissues and geometries, and consequently the voltages and currents, are substantially different. Since none of the observations and principles preclude the use of this approach in other comparable conditions (e.g., different waveforms, tissues, anatomical locations or geometries for the systems), the results of this study pave the road for the development of diagnostic and therapeutic systems using elongated flexible threadlike electronic implants that can be easily deployed by injection and powered by WPT based on HF volume conduction in limbs.

## REFERENCES

- [1] V. Parsonnet, J. Driller, D. Cook, and S. A. Rizvi, "Thirty-One Years of Clinical Experience with 'Nuclear-Powered' Pacemakers."
- [2] M. Han *et al.*, "Three-dimensional piezoelectric polymer microsystems for vibrational energy harvesting, robotic interfaces and biomedical implants," *Nat. Electron.*, vol. 2, no. 1, pp. 26–35, 2019, doi: 10.1038/s41928-018-0189-7.
- [3] A. Cadei, A. Dionisi, E. Sardini, and M. Serpelloni, "Kinetic and thermal energy harvesters for implantable medical devices and biomedical autonomous sensors," *Meas. Sci. Technol.*, vol. 25, p. 012003, 2014, doi: 10.1088/0957-0233/25/1/012003.
- [4] P. Nadeau *et al.*, "Prolonged energy harvesting for ingestible devices," *Nat. Biomed. Eng.*, vol. 1, no. 3, pp. 1–8, 2017, doi: 10.1038/s41551-016-0022.
- [5] D. Jiang *et al.*, "A 25-year bibliometric study of implantable energy harvesters and self-powered implantable medical electronics researches," *Mater. Today Energy*, vol. 16, pp. 100386–100386, 2020, doi: 10.1016/j.mtener.2020.100386.
- [6] R. Hinchet *et al.*, "Transcutaneous ultrasound energy harvesting using capacitive triboelectric technology," *Science*, vol. 365, no. 6452, pp. 491–494, 2019, doi: 10.1126/science.aan3997.
- [7] J. Thimot and K. L. Shepard, "Bioelectronic devices: Wirelessly powered implants," *Nat. Biomed. Eng.*, vol. 1, no. 3, pp. 1–2, 2017, doi: 10.1038/s41551-017-0051.
- [8] A. Auricchio *et al.*, "Feasibility, safety, and short-term outcome of leadless ultrasound-based endocardial left ventricular resynchronization in heart failure patients: Results of the Wireless Stimulation Endocardially for CRT (WiSE-CRT) study," *Europace*, vol. 16, no. 5, pp. 681–688, 2014, doi: 10.1093/europace/eut435.
- [9] P. Gutruf *et al.*, "Fully implantable optoelectronic systems for battery-free, multimodal operation in neuroscience research," *Nat. Electron.*, vol. 1, no. 12, pp. 652–660, 2018, doi: 10.1038/s41928-018-0175-0.
- [10] A. Abdo, M. Sahin, D. S. Freedman, E. Cevik, P. S. Spuhler, and M. S. Unlu, "Floating light-activated microelectrical stimulators tested in the rat spinal cord," *J. Neural Eng.*, vol. 8, no. 5, p. 056012, 2011, doi: 10.1088/1741-2560/8/5/056012.
- [11] J. Kim *et al.*, "Active photonic wireless power transfer into live tissues," *Proc. Natl. Acad. Sci. U. S. A.*, vol. 117, no. 29, pp. 16856–16863, 2020, doi: 10.1073/pnas.2002201117.
- [12] K. Mathieson *et al.*, "Photovoltaic retinal prosthesis with high pixel density," *Nat. Photonics*, vol. 6, pp. 391–397, 2012, doi: 10.1038/nphoton.2012.104.
- [13] H. Zhang *et al.*, "Wireless, battery-free optoelectronic systems as subdermal implants for local tissue oximetry," *Sci. Adv.*, vol. 5, no. 3, pp. eaaw0873–eaaw0873, 2019, doi: 10.1126/sciadv.aaw0873.
- [14] J. S. Ho *et al.*, "Wireless power transfer to deep-tissue microimplants," *Proc. Natl. Acad. Sci. U. S. A.*, vol. 111, no. 22, pp. 7974–9, 2014, doi: 10.1073/pnas.1403002111.
- [15] D. R. Agrawal *et al.*, "Conformal phased surfaces for wireless powering of bioelectronic microdevices," *Nat. Biomed. Eng.*, vol. 1, no. 3, p. 0043, 2017, doi: 10.1038/s41551-017-0043.
- [16] E. Y. Chow, Y. Ouyang, B. Beier, W. J. Chappell, and P. P. Irazoqui, "Evaluation of cardiovascular stents as antennas for implantable wireless applications," *IEEE Trans. Microw. Theory Tech.*, vol. 57, no. 10, pp. 2523–2532, 2009, doi: 10.1109/TMTT.2009.2029954.
- [17] R. Jegadeesan, K. Agarwal, Y. X. Guo, S. C. Yen, and N. V. Thakor, "Wireless Power Delivery to Flexible Subcutaneous Implants Using Capacitive Coupling," *IEEE Trans. Microw. Theory Tech.*, vol. 65, no. 1, pp. 280–292, 2017, doi: 10.1109/TMTT.2016.2615623.
- [18] R. Erfani, F. Marefat, A. M. Sodagar, and P. Mohseni, "Transcutaneous capacitive wireless power transfer (C-WPT) for biomedical implants," *Proc. - IEEE Int. Symp. Circuits Syst.*, pp. 4–7, 2017, doi: 10.1109/ISCAS.2017.8050940.
- [19] A. Aldaoud *et al.*, "Near-field wireless power transfer to stent-based biomedical implants," *IEEE J. Electromagn. RF Microw. Med. Biol.*, vol. 2, no. 3, pp. 193–200, 2018, doi: 10.1109/JERM.2018.2833386.
- [20] L. Becerra-Fajardo, M. Schmidbauer, and A. Ivorra, "Demonstration of 2 mm Thick Microcontrolled Injectable Stimulators Based on Rectification of High Frequency Current Bursts," *IEEE Trans. Neural Syst. Rehabil. Eng.*, vol. 25, no. 8, pp. 1343–1352, 2017, doi: 10.1109/TNSRE.2016.2623483.
- [21] P. Chen, H. Yang, R. Luo, and B. Zhao, "A Tissue-Channel Transcutaneous Power Transfer Technique for Implantable Devices," *IEEE Trans. Power Electron.*, vol. 33, no. 11, pp. 9753–9761, 2018, doi: 10.1109/TPEL.2018.2791966.
- [22] M. Tudela-Pi, L. Becerra-Fajardo, A. Garcia-Moreno, J. Minguillon, and A. Ivorra, "Power Transfer by Volume Conduction: In Vitro Validated Analytical Models Predict DC Powers above 1 mW in Injectable Implants," *IEEE Access*, 2020, doi: 10.1109/ACCESS.2020.2975597.
- [23] R. Sedehi *et al.*, "A Wireless Power Method for Deeply Implanted Biomedical Devices via Capacitively Coupled Conductive Power Transfer," *IEEE Trans. Power Electron.*, vol. 36, no. 2, pp. 1870–1882, 2021, doi: 10.1109/TPEL.2020.3009048.
- [24] C. Lee *et al.*, "A Miniaturized Wireless Neural Implant with Body-Coupled Data Transmission and Power Delivery for Freely Behaving Animals," in *2022 IEEE International Solid-State Circuits Conference (ISSCC)*, Feb. 2022, vol. 65, pp. 1–3, doi: 10.1109/ISSCC42614.2022.9731733.
- [25] A. B. Amar, A. B. Kouki, and H. Cao, "Power approaches for implantable medical devices," *Sens. Switz.*, vol. 15, no. 11, pp. 28889–28914, 2015, doi: 10.3390/s151128889.
- [26] A. Kim, M. Ochoa, R. Rahimi, and B. Ziaie, "New and Emerging Energy Sources for Implantable Wireless Microdevices," *IEEE Access*, vol. 3, pp. 89–98, 2015, doi: 10.1109/ACCESS.2015.2406292.
- [27] G. L. Barbruni, P. Motto Ros, D. Demarchi, S. Carrara, and D. Ghezzi, "Miniaturised Wireless Power Transfer Systems for Neurostimulation: A Review," *IEEE Trans. Biomed. Circuits Syst.*, pp. 1–20, 2020, doi: 10.1109/tbcas.2020.3038599.
- [28] K. Agarwal, N. V. Thakor, R. Jegadeesan, Y.-X. Guo, and N. V. Thakor, "Wireless Power Transfer Strategies for Implantable Bioelectronics," *IEEE Rev. Biomed. Eng.*, vol. 10, pp. 136–161, 2017, doi: 10.1109/RBME.2017.2683520.
- [29] A. Ivorra, L. Becerra-Fajardo, and Q. Castellví, "In vivo demonstration of injectable microstimulators based on charge-balanced rectification of epidermally applied currents," *J. Neural Eng.*, vol. 12, no. 6, 2015, doi: 10.1088/1741-2560/12/6/066010.
- [30] A. Vander Vorst, A. Rosen, and Y. Kotsuka, "RF/Microwave Interaction Mechanisms in Biological Materials," in *RF/Microwave Interaction with Biological Tissues*, John Wiley & Sons, Inc., 2006.

- [31] W. J. Tomlinson, S. Banou, S. Blechinger-Slocum, C. Yu, and K. R. Chowdhury, "Body-guided galvanic coupling communication for secure biometric data," *IEEE Trans. Wirel. Commun.*, vol. 18, no. 8, pp. 4143–4156, 2019, doi: 10.1109/TWC.2019.2921964.
- [32] M. Seyedli, B. Kibret, D. T. H. Lai, and M. Faulkner, "A survey on intrabody communications for body area network applications," *IEEE Trans. Biomed. Eng.*, 2013, doi: 10.1109/TBME.2013.2254714.
- [33] D. P. Lindsey, E. L. McKee, M. L. Hull, and S. M. Howell, "A new technique for transmission of signals from implantable transducers," *IEEE Trans. Biomed. Eng.*, vol. 45, no. 5, pp. 605–613, 1998, doi: 10.1109/10.668751.
- [34] D. Sharma, M. A. Miller, C. Palaniswamy, J. S. Koruth, S. R. Dukkupati, and V. Y. Reddy, "The leadless cardiac pacemaker conductive communication," *JACC Clin. Electrophysiol.*, vol. 1, no. 4, pp. 335–336, 2015, doi: 10.1016/j.jacep.2015.05.007.
- [35] S. A. Hackworth, "Design, optimization, and implementation of a volume conduction energy transfer platform for implantable devices," PhD Thesis, University of Pittsburgh, 2010.
- [36] W. Zhu, W. Fang, S. Zhan, Y. Zhou, Q. Gao, and X. Gao, "Volume conduction energy transfer for implantable devices," *J. Biomed. Res.*, vol. 27, no. 6, pp. 509–514, 2013, doi: 10.7555/JBR.27.20130090.
- [37] R. Erfani, F. Marefat, A. M. Sodagar, and P. Mohseni, "Modeling and characterization of capacitive elements with tissue as dielectric material for wireless powering of neural implants," *IEEE Trans. Neural Syst. Rehabil. Eng.*, vol. 26, no. 5, pp. 1093–1099, 2018, doi: 10.1109/TNSRE.2018.2824281.
- [38] A. M. Sodagar and P. Amiri, "Capacitive coupling for power and data telemetry to implantable biomedical microsystems," *2009 4th Int. IEEEEMBS Conf. Neural Eng. NER 09*, pp. 411–414, 2009, doi: 10.1109/NER.2009.5109320.
- [39] R. Narayanamoorthi, "Modeling of Capacitive Resonant Wireless Power and Data Transfer to Deep Biomedical Implants," *IEEE Trans. Compon. Packag. Manuf. Technol.*, vol. 9, no. 7, pp. 1253–1263, 2019, doi: 10.1109/TCPMT.2019.2922046.
- [40] J. W. Mackenzie, J. C. Schuder, and H. E. Stephenson, "Radio-frequency energy transport into the body," *J. Surg. Res.*, vol. 7, no. 3, pp. 133–144, 1967, doi: 10.1080/15411796.2011.585906.
- [41] M. A. Akram, K.-W. Yang, and S. Ha, "Duty-Cycled Wireless Power Transmission for Millimeter-Sized Biomedical Implants," *Electronics*, vol. 9, no. 12, Art. no. 12, Dec. 2020, doi: 10.3390/electronics9122130.
- [42] R. Erfani, F. Marefat, A. M. Sodagar, and P. Mohseni, "Modeling and Experimental Validation of a Capacitive Link for Wireless Power Transfer to Biomedical Implants," *IEEE Trans. Circuits Syst. II Express Briefs*, vol. 65, no. 7, pp. 923–927, 2018, doi: 10.1109/TCSIL.2017.2737140.
- [43] N. Modak *et al.*, "EQS Res-HBC: A 65-nm Electro-Quasistatic Resonant 5–240  $\mu$ W Human Whole-Body Powering and 2.19  $\mu$ W Communication SoC With Automatic Maximum Resonant Power Tracking," *IEEE J. Solid-State Circuits*, vol. 57, no. 3, pp. 831–844, Mar. 2022, doi: 10.1109/JSSC.2022.3142177.
- [44] A. Datta, M. Nath, D. Yang, and S. Sen, "Advanced Biophysical Model to Capture Channel Variability for EQS Capacitive HBC," *IEEE Trans. Biomed. Eng.*, vol. 68, no. 11, pp. 3435–3446, Nov. 2021, doi: 10.1109/TBME.2021.3074138.
- [45] J. Li, Y. Dong, J. H. Park, L. Lin, T. Tang, and J. Yoo, "Body-Area Powering With Human Body-Coupled Power Transmission and Energy Harvesting ICs," *IEEE Trans. Biomed. Circuits Syst.*, vol. 14, no. 6, pp. 1263–1273, Dec. 2020, doi: 10.1109/TBCAS.2020.3039191.
- [46] Y. Dong *et al.*, "Body-Coupled Power Transceiver with Node-Specific Body-Area Powering," in *ESSCIRC 2021 - IEEE 47th European Solid State Circuits Conference (ESSCIRC)*, Sep. 2021, pp. 423–426, doi: 10.1109/ESSCIRC53450.2021.9567745.
- [47] International Commission on Non-Ionizing Radiation Protection, "Guidelines for limiting exposure to electromagnetic fields (100 kHz to 300 GHz)," *Health Phys.*, vol. 118, no. 5, pp. 483–524, 2020, doi: 10.1097/HP.0000000000001210.
- [48] I. of Electrical and E. Engineers, *IEEE Std C95.1™-2019: IEEE Standard for Safety Levels with Respect to Human Exposure to Electric, Magnetic, and Electromagnetic Fields, 0 Hz to 300 GHz*. Institute of Electrical and Electronics Engineers, 2019. doi: 10.1109/IEEESTD.2019.8859679.
- [49] Bureau Radiocommunication - International Telecommunication Union, "Radio Regulations Articles Edition of 2020," 2020.
- [50] L. Becerra-Fajardo, M. Tudela-Pi, and A. Ivorra, "Two-Port Networks to Model Galvanic Coupling for Intrabody Communications and Power Transfer to Implants," *2018 IEEE Biomed. Circuits Syst. Conf. BioCAS*, pp. 1–4, 2018, doi: 10.1109/BIOCAS.2018.8584691.
- [51] M. Tudela-Pi, J. Minguiillon, L. Becerra-Fajardo, and A. Ivorra, "Volume Conduction for Powering Deeply Implanted Networks of Wireless Injectible Medical Devices: A Numerical Parametric Analysis," *IEEE Access*, vol. 9, pp. 100594–100605, 2021, doi: 10.1109/ACCESS.2021.3096729.
- [52] D. J. Weber *et al.*, "BIONic WalkAide for correcting foot drop," *IEEE Trans. Neural Syst. Rehabil. Eng.*, vol. 13, no. 2, pp. 242–246, 2005, doi: 10.1109/TNSRE.2005.847385.
- [53] J. C. Carr, W. Richard Fright, and R. K. Beatson, "Surface interpolation with radial basis functions for medical imaging," *IEEE Trans. Med. Imaging*, vol. 16, no. 1, pp. 96–107, 1997, doi: 10.1109/42.552059.
- [54] D. A. Field, "Laplacian smoothing and Delaunay triangulations," *Commun. Appl. Numer. Methods*, vol. 4, no. 6, pp. 709–712, 1988, doi: 10.1002/cnm.1630040603.
- [55] P. Haggall *et al.*, "IT'IS Database for thermal and electromagnetic parameters of biological tissues, Version 4.0," *IT'IS*, 2018.
- [56] D. U. Furrer and S. L. Semiatin, Eds., "Physical Data on the Elements and Alloys," in *Fundamentals of Modeling for Metals Processing*, vol. 22A, ASM International, 2009, pp. 0–0. doi: 10.31399/asm.hb.v22a.a0005445.
- [57] A. U. M, E. Anthony, and E. Godspower, "Electrical Properties of Enamel Wire Insulation," *Int. J. Trend Sci. Res. Dev.*, vol. Volume-3, no. Issue-2, pp. 803–806, 2019, doi: 10.31142/ijtsrd21450.
- [58] W. H. Hayt, J. Kemmerly, and S. M. Durbin, "Two-port networks," in *Engineering Circuit Analysis*, 8th ed., New York: McGraw-Hill, 2012, pp. 687–732.
- [59] IEC/IEEE International, "Determining the peak spatial-average specific absorption rate (SAR) in the human body from wireless communications devices, 30 MHz to 6 GHz - Part 1: General requirements for using the finite-difference time-domain (FDTD) method for SAR calculations," *IECIEEE 62704-1*, pp. 1–86, 2017, doi: 10.1109/IEEESTD.2017.8088404.
- [60] J. Olivo, S. Carrara, and G. D. Micheli, "Energy Harvesting and Remote Powering for Implantable Biosensors," *IEEE Sens. J.*, vol. 11, no. 7, pp. 1573–1586, 2011, doi: 10.1109/jsen.2010.2085042.
- [61] W. J. Heetderks, "RF Powering of Millimeter- and Submillimeter-Sized Neural Prosthetic Implants," *IEEE Trans. Biomed. Eng.*, vol. 35, no. 5, pp. 323–327, 1988, doi: 10.1109/10.1388.
- [62] A. Ibrahim, M. Meng, and M. Kiani, "A Comprehensive Comparative Study on Inductive and Ultrasonic Wireless Power Transmission to Biomedical Implants," *IEEE Sens. J.*, vol. 18, no. 9, pp. 3813–3826, 2018, doi: 10.1109/JSEN.2018.2812420.
- [63] B. C. Johnson *et al.*, "StimDust: A 6.5mm<sup>3</sup>, wireless ultrasonic peripheral nerve stimulator with 82% peak chip efficiency," 2018. doi: 10.1109/CICC.2018.8357047.
- [64] D. R. Agrawal *et al.*, "Conformal phased surfaces for wireless powering of bioelectronic microdevices," *Nat. Biomed. Eng.*, vol. 1, 2017, doi: 10.1038/s41551-017-0043.
- [65] A. Basir and H. Yoo, "Efficient Wireless Power Transfer System With a Miniaturized Quad-Band Implantable Antenna for Deep-Body Multitasking Implants," *IEEE Trans. Microw. Theory Tech.*, vol. 68, no. 5, pp. 1943–1953, May 2020, doi: 10.1109/TMTT.2020.2965938.
- [66] D. Ahn and M. Ghovanloo, "Optimal Design of Wireless Power Transmission Links for Millimeter-Sized Biomedical Implants," *IEEE Trans. Biomed. Circuits Syst.*, vol. 10, no. 1, pp. 125–137, 2016, doi: 10.1109/TBCAS.2014.2370794.
- [67] A. K. RamRakhyani, S. Mirabbasi, and M. Chiao, "Design and optimization of resonance-based efficient wireless power delivery systems for biomedical implants," *IEEE Trans. Biomed. Circuits Syst.*, vol. 5, no. 1, pp. 48–63, 2011, doi: 10.1109/TBCAS.2010.2072782.
- [68] D. K. Freeman *et al.*, "A sub-millimeter, inductively powered neural stimulator," *Front. Neurosci.*, vol. 11, no. NOV, pp. 1–12, 2017, doi: 10.3389/fnins.2017.00659.
- [69] T. Campi, S. Cruciani, V. De Santis, F. Maradei, and M. Feliziani, "Near Field Wireless Powering of Deep Medical Implants," *Energies*, vol. 12, no. 14, 2019, doi: 10.3390/en12142720.



# Powering Electronic Implants by High Frequency Volume Conduction: In Human Validation

Jesus Minguillon, Marc Tudela-Pi, Laura Becerra-Fajardo, Enric Perera-Bel, Antonio J. del-Ama, Ángel Gil-Agudo, Álvaro Megía-García, Aracelys García-Moreno, Antoni Ivorra

## SUPPLEMENTARY MATERIAL

### SA. Tapered Cosine Window

To minimize the contribution of the harmonics generated by windowing the sinusoidal waveform, the applied bursts were smoothed with a tapered cosine window. This window is defined as

$$w(t) = \begin{cases} \frac{1}{2} \left[ 1 - \cos\left(\frac{2\pi t}{rB}\right) \right], & 0 \leq t \leq \frac{r}{2}B \\ 1, & \frac{r}{2}B \leq t \leq B - \frac{r}{2}B \\ \frac{1}{2} \left[ 1 - \cos\left(\frac{2\pi t}{rB} - \frac{2\pi}{r}\right) \right], & B - \frac{r}{2}B \leq t \leq B \end{cases} \quad (S1)$$

where  $r$  is the cosine fraction and  $B$  is the burst duration (i.e., window duration). This window is a rectangular window with the first and last  $r/2$  percent of the time equal to parts of a cosine. The expression for a single smoothed burst with a sinusoid as the modulated waveform is

$$b(t) = v(t) \cdot w(t) = V_{\text{peak}} \cdot \sin(2\pi f t + \varphi) \cdot w(t), \quad (S2)$$

where  $V_{\text{peak}}$ ,  $f$  and  $\varphi$  are the amplitude, frequency and initial phase of the sinusoidal modulated waveform respectively. Therefore, the RMS voltage of the waveform during the burst ( $V_{\text{rms in burst}}$ ) is

$$V_{\text{rms in burst}} = \sqrt{\frac{1}{B} \int_0^B [v(t) \cdot w(t)]^2 dt}. \quad (S3)$$

If we assume  $\varphi = 0$  and  $rBf/2$  is an integer number higher than zero (which corresponds to our case), then

$$V_{\text{rms in burst}} = \frac{V_{\text{peak}}}{\sqrt{2}} \sqrt{1 - \frac{5}{8}r} = V_{\text{peak}} \cdot k, \quad (S4)$$

where  $k$  is a constant that depends on the cosine fraction  $r$ . The RMS voltage of the waveform ( $V_{\text{rms}}$ ) is

$$V_{\text{rms}} = V_{\text{peak}} \cdot k \sqrt{FB}, \quad (S5)$$

where  $FB$  is the duty cycle, being  $F$  and  $B$  the repetition frequency and the duration of the bursts, respectively. Therefore, for power calculation, a scaling factor  $k\sqrt{FB}$  must be applied to transform amplitude values into RMS values for the applied waveform. A cosine fraction  $r = 0.5$  was used, thus  $k = \sqrt{11/32}$ . A smoothed burst ( $V_{\text{peak}} = 1$  V,  $f = 6.78$  MHz,  $B = 100$   $\mu$ s) is shown in Fig. S1.

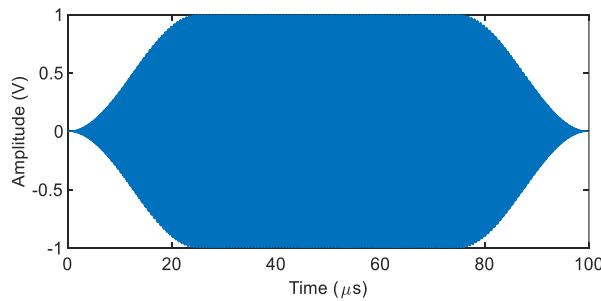


Fig. S1. Smoothed burst ( $V_{\text{peak}} = 1$  V,  $f = 6.78$  MHz,  $B = 100$   $\mu$ s) with tapered cosine window ( $r = 0.5$ ).

### SB. Dosimetric Reference Level

In terms of the electrostimulation effects, the IEEE safety standard [1] defines the dosimetric reference level (DRL) as the in situ electric field, and it is determined for frequencies between 0 Hz and 5 MHz. According to this, for continuous 6.78 MHz sinusoidal waveform, which is the carrier frequency of the sinusoidal voltage bursts used in this study, the DRL for electrostimulation mechanisms does not apply. However, the standard also provides limits for non-sinusoidal fields, as it is the case here. The standard indicates that the exposure waveform consisting of multiple frequencies must satisfy that

$$\sum_{0 \text{ MHz}}^{5 \text{ MHz}} \frac{A_i}{RL_i} \leq 1, \quad (S6)$$

where  $A_i$  is the magnitude of the  $i$ th Fourier component of the sinusoidal voltage bursts, and  $RL_i$  represents the in situ electric field restriction defined by the maximum allowed in situ electric field  $E_i$  for the  $i$ th Fourier component

$$E_i = \begin{cases} E_0, & f < f_e \\ E_0 \frac{f}{f_e}, & f \geq f_e \end{cases}, \quad (S7)$$

where  $E_0$  is the rheobase in situ field,  $f_e$  is the transition frequency, and  $f$  is the frequency of the  $i$ th Fourier component. For the scenario considered in this study, in which the sinusoidal voltage bursts are applied to the limbs,  $E_0$  is defined as 2.10 V<sub>rms</sub>/m, and  $f_e$  is defined as 3350 Hz.

From (S6) and (S7), two ranges are identified: a lower bound ( $f \leq 3350$  Hz) and an upper bound ( $5 \text{ MHz} \geq f > 3350$  Hz). Therefore,

$$\left( \sum_{0}^{3350 \text{ Hz}} \frac{A_i}{E_0} + \sum_{3350 \text{ Hz}}^{5 \text{ MHz}} \frac{A_i}{E_0 \frac{f_i}{f_e}} \right) \leq 1. \quad (S8)$$

The maximum peak electric field that could be applied by the voltage generator was calculated according to (S8) using MATLAB R2019a. The sinusoidal voltage burst waveform (carrier frequency = 6.78 MHz,  $B = 100 \mu\text{s}$  and  $F = 1$  kHz) was smoothed with a tapered cosine window created using the *tukeywin* function from MATLAB, with  $r = 0.5$ . A 0.1 s duration waveform was then generated using a sampling frequency of 100 Msps, and its discrete Fourier transform was calculated. After identifying the two ranges defined by (S8), their summation was computed having in mind the magnitude of the  $i$ th Fourier component, the rheobase in situ field, and the transition frequency. The resulting maximum peak electric field (i.e., the maximum in situ electric field to avoid electrostimulation) was approximately 227 MV/m.

### SC. Powering Electronic Devices

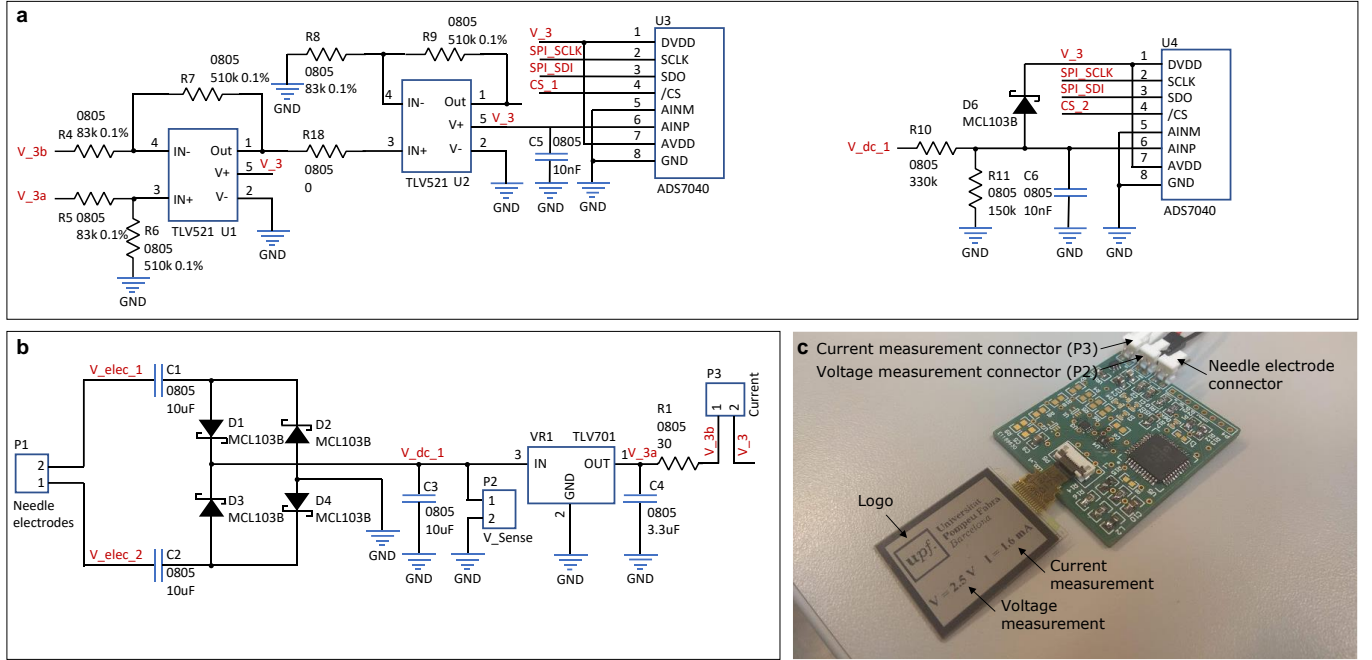
To illustrate the potential of volume conduction to power complex digital implants, a demonstrative electronic device was designed and manufactured using commercial off-the-shelf components (Fig. S2c). This electronic device was connected to the needle electrodes. The main function of this device was to show its input voltage and current by means of a 1.3" LCD screen (LS013B7DH05 from Sharp Corporation Sakai, Osaka Prefecture, Japan). The electronic device does not contain any power source and is composed of three subcircuits: 1) power stage, 2) sensing stage and 3) control unit and display.

The power stage consists of a dc-blocking capacitor for each electrode, followed by a bridge rectifier (diode MCL103B from Vishay Intertechnology, Malvern, PA, US), a smoothing capacitor (10  $\mu\text{F}$ ) that rectifies the picked-up high frequency voltage, and a linear voltage regulator (TLV701 from Texas Instruments, Dallas, TX, US) that fixes a voltage of 3.3 V (Fig. S2a).

The sensing stage is used to measure the input dc voltage and current. The voltage is measured across the smoothing capacitor that follows the diode bridge. The current is measured by acquiring the voltage drop across a shunt resistor (30  $\Omega$ ) located after the smoothing capacitor of the regulator's output. This voltage is amplified using two amplification stages (implemented with operational amplifiers TLV521 from Texas Instruments, Dallas, TX, US) that set a gain of 51 V/V. The voltages are digitized using two 8-bit analog-to-digital converters (ADS7040 from Texas Instruments, Dallas, TX, US). The result of the conversions is obtained by the control unit through a serial peripheral interface (SPI).

The control unit is based on an 8-bit, low-power microcontroller (PIC18LF47K42 from Microchip Technology Inc., Chandler, AZ, US) with a clock frequency set to 1 MHz. The microcontroller interrogates the ADCs every 10 ms and then updates the LCD screen (via SPI communication) with the acquired measurement. Both current (mA) and voltage (V) are shown on the screen with a resolution of 0.1 mA and 0.1 V, respectively (Fig. S2b). Approximately every 20 s the microcontroller refreshes the LCD and changes the logo that the LCD shows on its top. Two different logos can be displayed. Since the main purpose of this device was to show the potential of volume conduction to power complex digital circuits, the circuit was designed to minimize its power consumption at the expense of the measurement accuracy. That is the reason why the voltage and the current to calculate the power consumption were externally measured through the two 2-pin connectors P2 and P3 using the multimeters mentioned in Section

II.G. The electronic components were mounted on a 45 × 40 mm two-layers PCB (see Fig. S2c). The base material is FR-4 and its thickness is 1.55 mm. This device is similar to most implantable medical devices in terms of complexity and power consumption (few milliwatts), and far above to that of pacemakers, which is in the order of 10  $\mu$ W [2]. The actual power consumption was estimated by measuring dc voltage and dc current using two multimeters (38XR-A from Amprobe, Everett, WA, US).



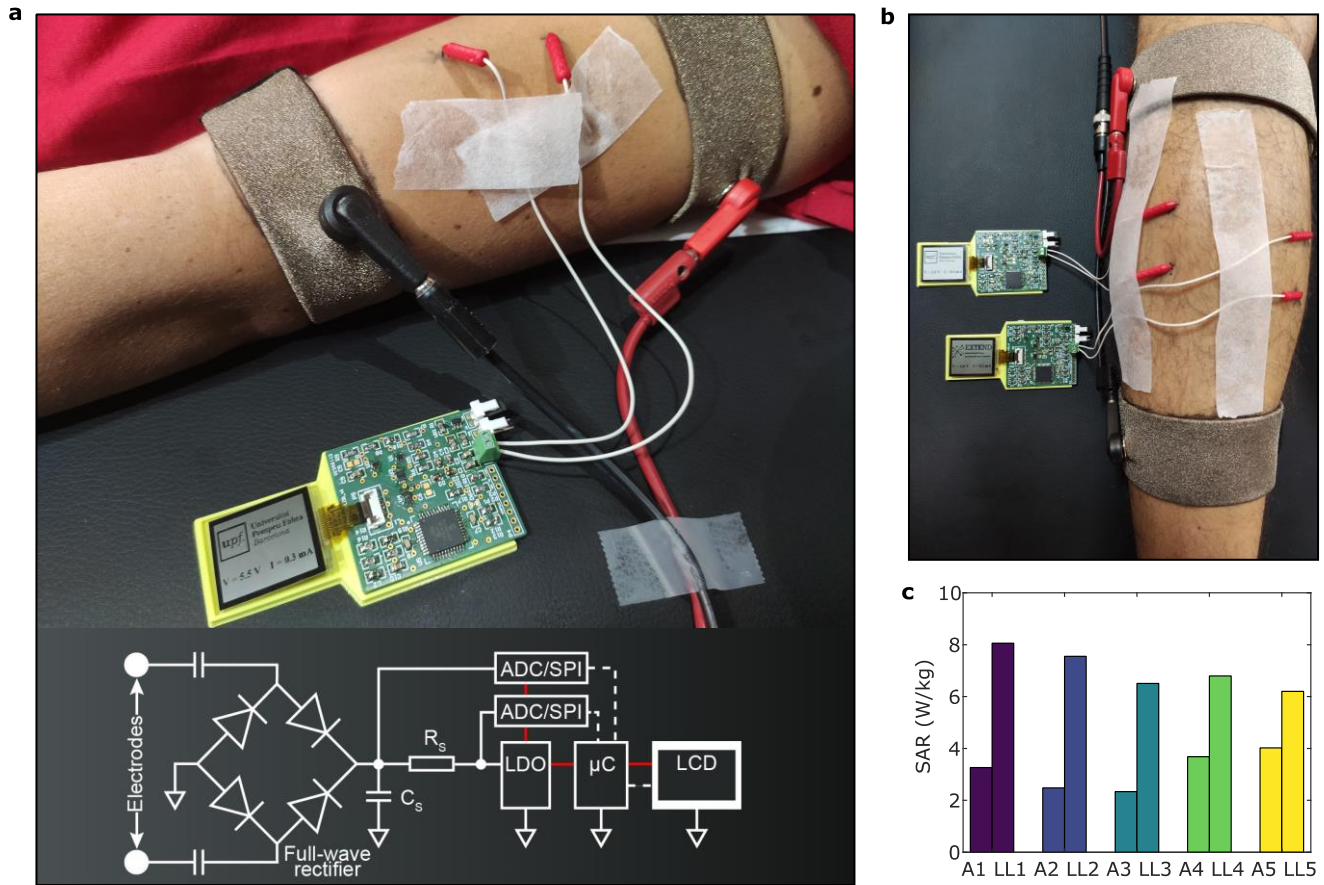


Fig. S3. Illustration of the capability of WPT based on volume conduction for safely powering electronic devices. (a) Picture of an electronic device, which is comparable to a medical implant in terms of circuit complexity and power consumption, being powered by volume conduction of high frequency current bursts (carrier frequency = 6.78 MHz, burst duration = 100  $\mu$ s, and repetition frequency = 1 kHz). (b) Two devices being simultaneously powered by the same current bursts. (c) Projected maximum SAR in tissues when the amplitude of the external voltage is sufficient for powering the electronic devices of this setup.

#### SE. Other Supplementary Figures

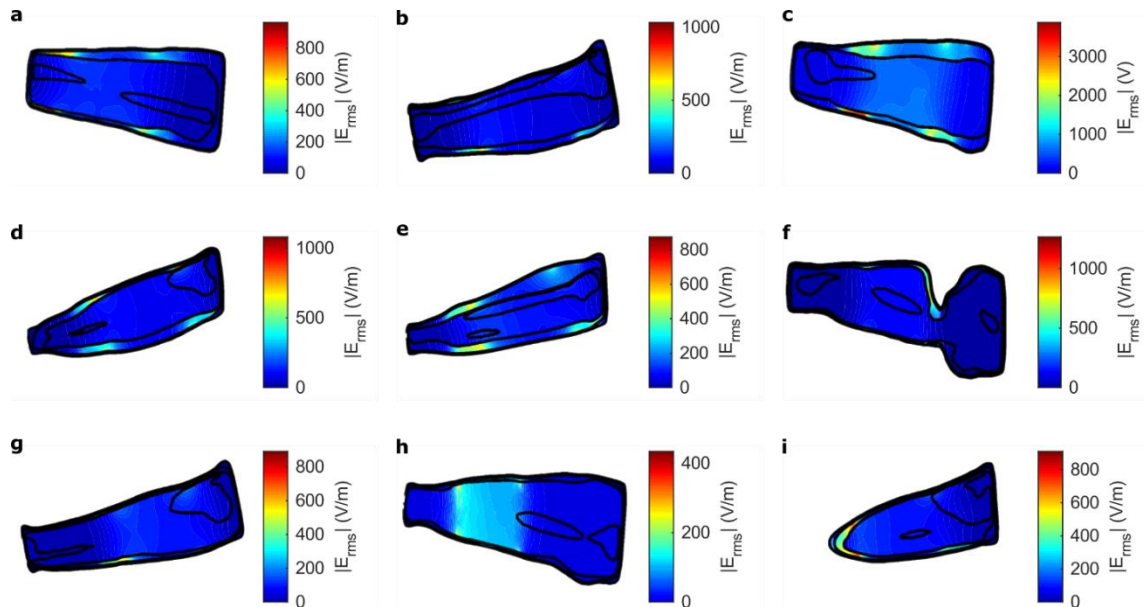


Fig. S4. Computed electric field distribution for each case. (a) Arm of P1 (A1). (b) Lower leg of P1 (LL1). (c) Arm of P2 (A2). (d) Lower leg of P2 (LL2). (e) Lower leg of P3 (LL3). (f) Arm of P4 (A4). (g) Lower leg of P4 (LL4). (h) Arm of P5 (A5). (i) Lower leg of P5 (LL5). The electric field distribution for the arm of P3 (A3) is reported in Fig. 6b.



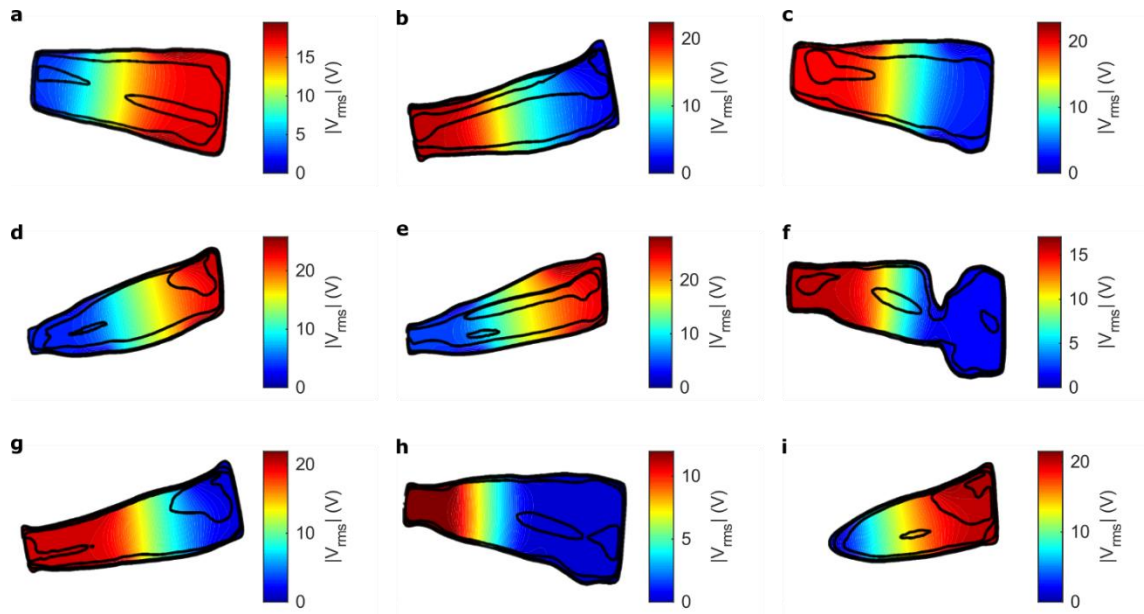


Fig. S5. Computed voltage distribution for each case. (a) Arm of P1 (A1). (b) Lower leg of P1 (LL1). (c) Arm of P2 (A2). (d) Lower leg of P2 (LL2). (e) Lower leg of P3 (LL3). (f) Arm of P4 (A4). (g) Lower leg of P4 (LL4). (h) Arm of P5 (A5). (i) Lower leg of P5 (LL5). The voltage distribution for the arm of P3 (A3) is reported in Fig. 6c.

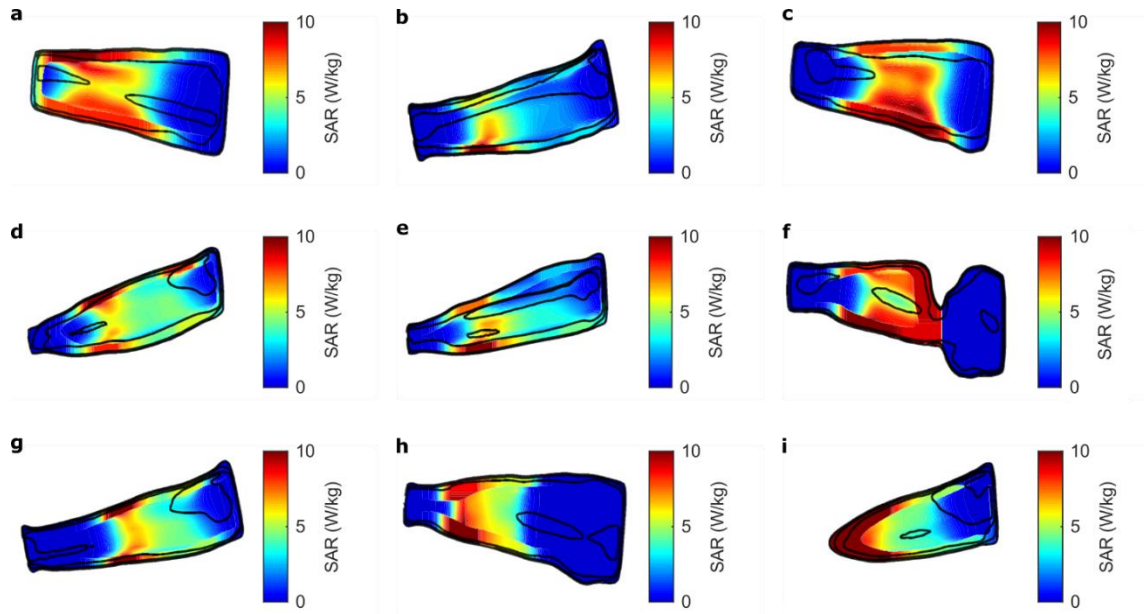


Fig. S6. Computed projected SAR distribution for each case. (a) Arm of P1 (A1). (b) Lower leg of P1 (LL1). (c) Arm of P2 (A2). (d) Lower leg of P2 (LL2). (e) Lower leg P3 (LL3). (f), Arm of P4 (A4). (g) Lower leg of P4 (LL4). (h) Arm of P5 (A5). (i) Lower leg of P5 (LL5). The projected SAR distribution for the arm of P3 (A3) is reported in Fig. 6d.

#### SUPPLEMENTARY REFERENCES

- [1] I. of Electrical and E. Engineers, IEEE Std C95.1™-2019: IEEE Standard for Safety Levels with Respect to Human Exposure to Electric, Magnetic, and Electromagnetic Fields, 0 Hz to 300 GHz. Institute of Electrical and Electronics Engineers, 2019. doi: 10.1109/IEEESTD.2019.8859679.
- [2] J. S. Ho et al., “Wireless power transfer to deep-tissue microimplants,” Proc. Natl. Acad. Sci. U. S. A., vol. 111, no. 22, pp. 7974–9, 2014, doi: 10.1073/pnas.1403002111.